AlGaAs two by two pixel detector for electron spectroscopy in space environments

Article (Accepted Version)

AlGaAs two by two pixel detector for electron spectroscopy in space environments

M.D.C. Whitaker*, S. Zhao, G. Lioliou, S. Butera, and A.M. Barnett
Space Research Group, Sch. of Engineering and Informatics, University of Sussex, Falmer, Brighton, BN1 9QT, UK

Abstract
A prototype monolithic 2 × 2 square pixel $Al_{0.2}Ga_{0.8}As$ p^+-i-n^+ mesa photodiode array (each photodiode of area 200 µm by 200 µm, with a 3 µm i layer) has been investigated for its utility as a detector for direct detection electron (β^- particle) spectroscopy. Each photodiode was electrically characterised and its response to illumination from a ^{63}Ni radioisotope β^- particle source was investigated at 20 °C. The percentage of electron energy absorbed in the active layer (i layer), E_{abs}, of the photodiode and the spectrum expected to be detected, were calculated via Monte Carlo simulations. Comparisons between the simulated and detected ^{63}Ni β^- particle spectra are presented and demonstrate uniformity in response across the two by two pixel array. The percentage of electron energy absorbed in the active layer of the detector was at a maximum of 0.53 ± 0.04 for electrons with an energy of 38 keV; the percentage of electron energy absorbed in the active layer of the detector reduced to 0.29 ± 0.02 at 66 keV.

To increase the percentage of electron energy absorbed in the active layer of the detector at high energies, inactive Al absorption layers placed atop the detecting structure were investigated as part of the modelling work. These additional Al layers partially attenuated the β^- particles' energy, thus reducing the incident particles' energy to values more readily detected by the relatively thin photodiode. Al layers of 20 µm, 100 µm, and 500 µm thickness were investigated and found, by modelling, to increase the percentage of electron energy absorbed in the active layer of such a spectrometer by 22 % at 100 keV; 46 % at 200 keV; and 20 % at 500 keV, respectively.

Keywords
AlGaAs; Electron detector; Spectroscopy; Photodiode; Array; Semiconductor

1. Introduction

Space-borne electron spectrometers are used to study planetary magnetospheres, atmospheres, and surfaces, and their associated interactions with the solar wind and other forms of ionising radiation [1]. Efforts to understand such interactions have motivated considerable research efforts e.g. at Mercury [2], Jupiter [3], and Pluto [4]. However, present understanding is still far from complete [5]. As such, there is demand for electron spectrometers that can not only withstand the harsh environments of space, but also provide improved spectral and spatial resolutions in order to elucidate planetary and solar system processes.

Today, most semiconductor electron detecting instruments use Si detectors to determine the energies and, sometimes angular distributions, of incoming electrons. In many cases, the performance of Si as an electron detecting material is excellent; however, in high temperature (≥ 20 °C) and intense radiation environments (such as those experienced during space missions) other materials may be preferable.

Radiation detectors made from wide bandgap materials, such as $Al_xGa_{1-x}As$ [6][7][8], can possess superior resolutions at high temperature (≥ 20 °C) in comparison to Si detectors of comparable geometry. This is a consequence of the relatively wide bandgap of $Al_xGa_{1-x}As$ (1.67 eV for $Al_{0.2}Ga_{0.8}As$ [9] cf. 1.1 eV for Si [10]), which could lower thermally induced leakage currents [10] and consequently, lower parallel white noise contributions [11]. This benefit could aid in the exploration of high temperature environments found in space, such as those at Mercury (e.g. ≈ 400 °C [12]) and at comets when they are in the inner solar system (e.g. 87 °C at Halley's comet at a distance of 0.8 AU [13]), where current Si detectors are unable to operate without cooling. Si is also susceptible to radiation damage, causing degradation in spectrometer energy resolution over time within intense radiation environments (such environments are commonly encountered by space science instrumentation [14] [15]). $Al_xGa_{1-x}As$ solar cells are expected to have better radiation hardness [16][17][18], which may also apply to $Al_xGa_{1-x}As$ radiation detectors, prolonging spectrometer lifetimes compared with those that use Si detectors. These features are of particular interest for space science missions to study the Jovian [19] [20] and Saturnian [21] plasma environments, where background radiation doses can be particularly intense (e.g. 200 krad per day [22]).

Previously, results characterising prototype single pixel $Al_xGa_{1-x}As$ photodiodes of various Al concentration have been reported, with investigations primarily focused on soft X-ray photon detection. Single pixel

* Corresponding author, E-mail address: M.Whitaker@sussex.ac.uk

$Al_{0.8}Ga_{0.2}As$ circular mesa p^+-i-n^+ photodiodes (400 µm diameter, 1.7 µm i layer) [7] and $Al_{0.2}Ga_{0.8}As$ circular mesa p^+-i-n^+ photodiodes (200 µm diameter, 3 µm i layer) [23] have been characterised as soft X-ray photon counting detectors at room temperature (20 °C). Temperature dependence studies of $Al_xGa_{1-x}As$ detectors with these Al concentrations have also been reported [24][25]. Spectroscopic particle counting electron (β^- particle) spectroscopy has been reported using a single pixel $Al_{0.8}Ga_{0.2}As$ circular mesa p^+-i-n^+ photodiodes (400 µm diameter, 1 µm i layer) operated at 20 °C [26].

In the present work, $Al_{0.2}Ga_{0.8}As$ photodiodes were investigated and characterised for the first time as direct detection electron (β^- particle) detectors for particle counting spectroscopy. The work used a custom 2 × 2 square pixel $Al_{0.2}Ga_{0.8}As$ photodiode array originally intended as a developmental prototype for X-ray detection [27]. To investigate their response to illumination with β^- particles, the detector array was illuminated with a 182 MBq (134 MBq, taking into account self-absorption) ^{63}Ni radioisotope β^- particle source which consisted of a 7 mm × 7 mm, 3 µm thick, active ^{63}Ni layer, electroplated onto an ~50 µm thick inactive Ni foil substrate, and covered with a protective 1 µm thick inactive electroplated Ni overlayer.

2. Detector design

An $Al_{0.2}Ga_{0.8}As$ p^+-i-n^+ structure was grown to the authors' specifications at the Engineering and Physics Sciences Research Council (EPSRC) National Centre for III-V Technologies, Sheffield, UK, by metalorganic vapour phase epitaxy (MOVPE) on a commercial GaAs n^+ substrate. The layer details are summarised in Table 1. A four pixel (2 × 2) array of square, 200 µm × 200 µm, mesa structures was formed using 1:1:1 H_3PO_4:H_2O_2:H_2O solution followed by 10 s in 1:8:80 H_2SO_4:H_2O_2:H_2O solution. An Ohmic contact, consisting of 20 nm InGe and 200 nm Au, was evaporated onto the rear of the substrate, and an Ohmic top contact of 20 nm Ti and 200 nm Au was evaporated onto the p^+ side of each mesa device; the devices were unpassivated. Fig. 1 illustrates the top-down view of the $Al_{0.2}Ga_{0.8}As$ p^+-i-n^+ pixels. For convenience the pixels have been labelled D1, D2, D3, and D4. The p^+ metal top contact covers 50 % of each pixel's surface. The devices were packaged in a TO-5 can [28], a standardised metal semiconductor package. General electrical characterisation of the array was reported in ref. [27]; before obtaining the new β^- particle spectra presented in this new work, each pixel's electrical characteristics (leakage current and capacitance) were measured again as per ref. [27]. The array's electrical performance was identical to that already reported.

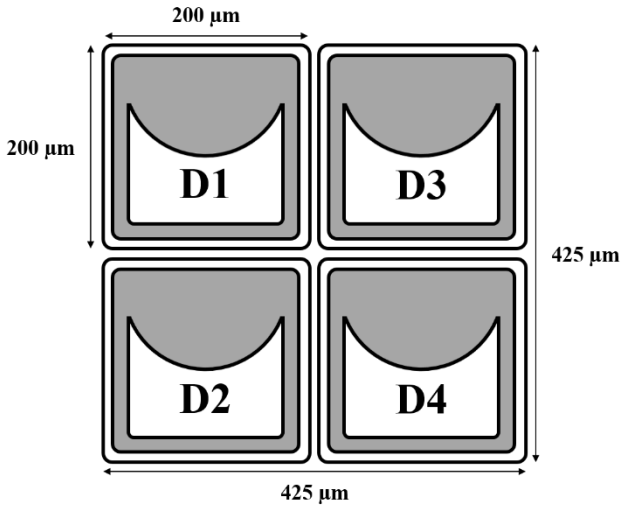

Fig. 1. Schematic top-down of the array (not to scale).

Table 1. Layer details of the $Al_{0.2}Ga_{0.8}As$ p^+-i-n^+ structure from which the devices were fabricated.

Material	Dopant	Dopant type	Thickness (µm)	Doping density (cm^{-3})
GaAs	Be	p	0.01	1×10^{19}
$Al_{0.2}Ga_{0.8}As$	Be	p	0.5	2×10^{18}
$Al_{0.2}Ga_{0.8}As$			3	Undoped
$Al_{0.2}Ga_{0.8}As$	Si	n	1	2×10^{18}
GaAs n^+ substrate				

3. Percentage of electron energy absorbed by the detector

The Monte Carlo simulation program CASINO [29][30], with which electron trajectories in solids can be simulated, was used to predict the percentage of electron energy, E_{abs}, absorbed in the active region (i layer) of

the photodiodes across the energy range 1 keV to 66 keV in 1 keV steps. The percentage of electron energy absorbed in the i layer was calculated by the ratio between the total electron energy deposited in the active layer and the total electron energy incident on a single photodiode's face, where simulations informed the values used in this calculation. Two sets of simulations, each using 4000 electrons, were performed at each electron energy. The first set was simulated as incident upon a portion of a pixel's face which was not covered by the top metal contact (the so called window). The second set was simulated as incident upon a portion of a pixel's face which was covered by the top metal contact. The results of the simulations were then combined in the appropriate proportions according to the areas covered and uncovered by the contact. In each set of simulations, the GaAs p^+ layer, the p^+ layer, the n^+ layer, and the substrate of the $Al_{0.2}Ga_{0.8}As$ p^+-i-n^+ mesa structure, were considered to be inactive; i.e. only charge created by electrons in the undoped region (i layer) was assumed to be usefully absorbed. One computer, with an Intel i7-6700 (4 cores, 3.40 GHz) processor and 32 GB of random access memory, was used to perform the simulations. CASINO was configured to use its Mott by interpolation model; the ionisation potential was set to Joy & Luo [32]; the random number generator was set to Press et al. [33]; the effective section ionisation was set to Casnati et al. [34]; the direction cosine was set to Hovington et al. [29]. Electrons were simulated as being incident at 90 ° to the photodiode's face at the start of their track through the detector. The electron beam width was set to 1 nm. Secondary electron generation was not included in the simulations. The same CASINO settings and presently reported methodology were used in refs [35], [36], and [37], to simulate similar situations in GaAs, SiC, and InGaP electron detectors. Fig. 2 presents the percentage of electron energy absorbed in the photodiode, predicted from these simulations.

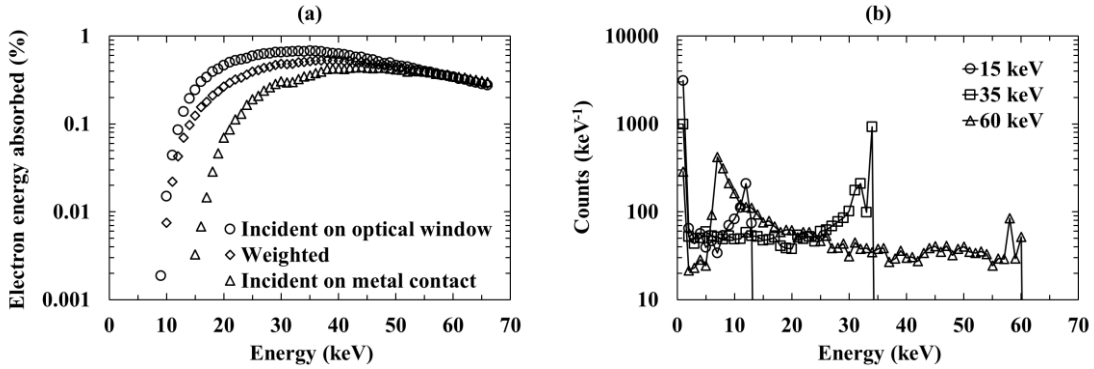

Fig. 2. a) Percentage of electron energy absorbed in the active layer (i layer) of the $Al_{0.2}Ga_{0.8}As$ p^+-i-n^+ mesa photodiode structure for electrons incident on the window (circles), weighted case for actual contact coverage of the pixel (diamonds), and electrons incident on the metal contact (triangles), as a function of electron energy, at 20 °C, as determined by Monte Carlo simulations. The associated uncertainties were smaller than the symbols. Fig. 2 b) number of electrons absorbed within the active layer of the $Al_{0.2}Ga_{0.8}As$ p^+-i-n^+ mesa photodiode structure, taking into account the actual contact coverage of the pixel, as a function of electron energy for 4,000 incident electrons of energy 15 keV (circles), 35 keV (squares), and 60 keV (triangles), at 20 °C, as determined by Monte Carlo simulations. Black lines have been included as guides for the eyes.

When electrons were incident upon the window of a pixel, the percentage of electron energy absorbed in the i layer increased with increasing electron energy up to ≈ 33 keV (= 0.68 ± 0.03). When electrons were incident upon the top metal contact of the detector, the percentage of electron energy absorbed in the i layer increased with increasing electron energy up to ≈ 44 keV (= 0.44 ± 0.02). The weighted percentage of electron energy absorbed in the i layer (i.e. assuming uniform illumination of the $Al_{0.2}Ga_{0.8}As$ p^+-i-n^+ mesa structure from the top) reached a maximum of 0.53 ± 0.04 at 38 keV. The increase of the weighted percentage of electron energy absorbed in the i layer with increasing electron energy up to 38 keV suggested that the absorption of electrons at low energies was limited by the absorption of electrons within the inactive top layers of the detector (top metal contacts and p^+ layers). Beyond an electron energy of 38 keV, the weighted percentage of electron energy absorbed in the i layer decreased, falling to 0.29 ± 0.02 at 66 keV. This suggested that the absorption of electrons with high energies (> 38 keV) was limited by the relative thinness (3 µm) of the active i layer, although losses in the inactive overlayers also played a part. A thicker i layer would be required for the optimal absorption of electrons with energies > 38 keV; for example, it was found that ≈ 5 µm and ≈ 13 µm thick $Al_{0.2}Ga_{0.8}As$ would fully absorb 95% of electrons with energies up to 38 keV and 66 keV respectively.

4. Expected and experimental measurements of ^{63}Ni β^- particle spectra

4.1 Expected spectrum incident on the detector

The β^- particle spectrum expected to be incident on the detector array as a result of illumination with the ^{63}Ni radioisotope β^- particle source was also simulated using the Monte Carlo simulation program CASINO [29][30]. Included in these simulations were the effects of self-absorption within the ^{63}Ni itself, as well as attenuation of

β^- particles as they passed through the radioisotope β^- particle source's inactive Ni overlayer (1 μm thick, density of 8.9 g cm^{-3} [31]) and the dry N_2 atmosphere (7 mm thick, density of 1.16 g cm^{-3} [38]) separating the ^{63}Ni radioisotope β^- particle source and the detector array. 66 independent simulations were conducted in steps of 1 keV, from 1 keV to 66 keV (the ^{63}Ni endpoint energy). The number of electrons simulated at each energy was dependent on the relative emission probability, P_i, of each β^- particle energy from ^{63}Ni as corrected for self-absorption in a 3 μm thick layer [39]. A total of 18,199,200 electrons were simulated. This number was selected to ensure sufficiently good statistics for interpretation of the data rather than to directly reflect the number of β^- particles which would be emitted from the source during the experimental accumulation of spectra reported in Section 4.2. A bank of 14 computers, each with an Intel i7-6700 (4 cores, 3.40 GHz) processor and 32 GB of random access memory, was used to perform the simulations. The presently reported methodology was the same as that used in refs [35], [36], and [37].

The computed trajectories of the simulated electrons were used to calculate the remaining energy of each electron after passing out of the ^{63}Ni itself and through the Ni overlayer and N_2 layer. The remaining energies of each of the 18,199,200 electrons were then binned into channels each of 1 keV width, thus providing the spectrum expected to be incident on the top face of the detector array. This spectrum is presented in Fig. 3. Particles which lost all of their energy before reaching the detector have been excluded from the spectrum.

The ^{63}Ni β^- particle spectrum predicted to be detected by each pixel was then calculated by combining the weighted histogram of deposited electron energies as a function of incident electron energy, produced by the Monte Carlo simulations used to predict the percentage of electron energy absorbed in the active region of the photodiodes (see Section 3), with the spectrum expected to be incident upon the detector. This is shown in Fig. 3, alongside the emitted spectrum and the spectrum incident on the detector. The spectrum predicted to be detected does not include the effects of Fano noise, spectrometer electronic noise, incomplete charge collection, or pixel edge effects. A key outcome of the simulations was the prediction of the spectrum's apparent endpoint energy which would be detected during the experimental measurements.

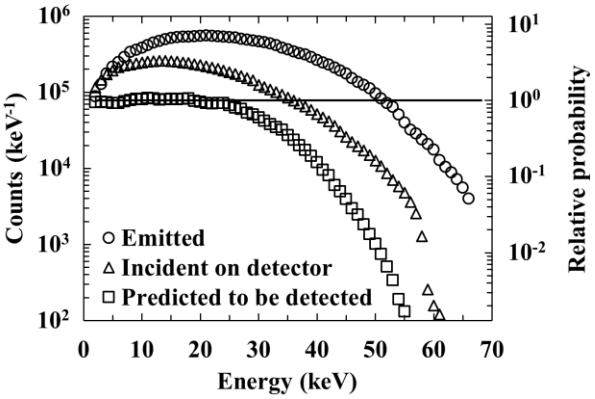

Fig. 3. Simulated ^{63}Ni β^- particle spectrum as emitted from the active material of the source including self-absorption (circles), incident on the top face of the detector (triangles) thus including attenuation in the inactive Ni overlayer and N_2 atmosphere, and predicted to be detected (squares). The relative probability axis refers to the predicted to be detected (squares) data series only. A relative probability of 1 (solid line) was assigned to the mean number of counts detected per channel within the broadly flat region (1 keV $\leq E \leq$ 20 keV) within the spectrum predicted to be detected. The associated uncertainties were smaller than the symbols.

4.2 ^{63}Ni β^- particle spectroscopy

Each pixel of the array was connected, in turn, to a single channel custom-made low-noise charge-sensitive preamplifier of feedback resistorless design, similar to that reported in ref. [40]. The output signal of the preamplifier was shaped using an Ortec 572A shaping amplifier, which was then connected to a multi-channel analyser (MCA) for digitisation. The temperature of the detector array and the preamplifier was 20 °C throughout the experiment. The detector array was operated in a dry N_2 environment for the duration of the measurements to eliminate any humidity related effects [41]. The ^{63}Ni radioisotope β^- particle source was placed 7 mm ± 1 mm above the detectors in the same dry N_2 environment. A spectrum accumulation live time of 1000 s and a shaping amplifier shaping time of 2 μs (optimal available shaping time for this detector array at 20 °C [27]) were used for each ^{63}Ni β^- particle spectrum, with a reverse bias of 30 V applied to each pixel. The pixels were fully depleted when operated in this bias condition. The spectra accumulated using each pixel are presented in Fig. 4. Each experimental ^{63}Ni β^- particle spectrum has been energy calibrated using the apparent endpoint energy determined from the simulations (see Section 4.1) taking into account the number of detected

counts and as such, the relative probability of detection, and the position of the zero energy noise peaks (not shown in the figures). The uncertainty in the apparent endpoint energy was ≤ 1 keV for each pixel. It was assumed that there was a linear variation of spectrometer output as a function of detected energy between the zero energy noise peak and the endpoint energy.

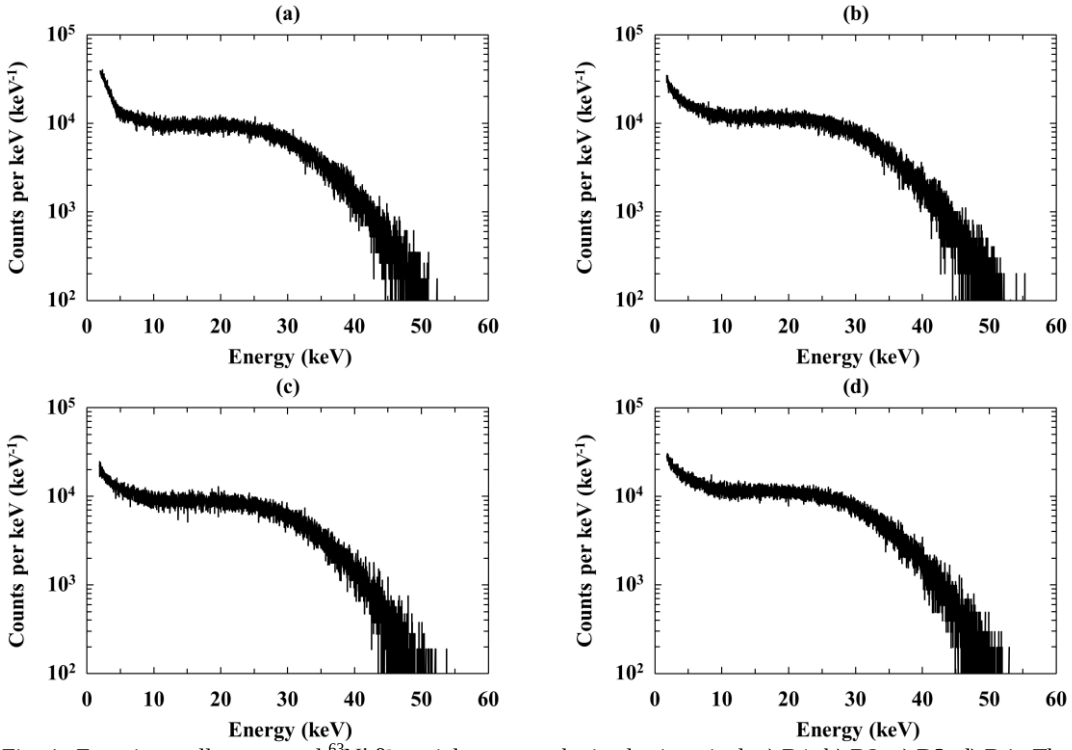

Fig. 4. Experimentally measured ^{63}Ni β^- particle spectra obtained using pixel: a) D1; b) D2; c) D3; d) D4. The accumulated spectra are presented in terms of counts per keV. The associated uncertainties were omitted for clarity.

The experimentally detected ^{63}Ni β^- particle spectra were compared with that predicted to be detected from the simulations. This comparison for pixel D1 is presented in Fig. 5. Comparable results were obtained for the other pixels. At low energies (≤ 11 keV), the difference between the simulated and measured ^{63}Ni β^- particle spectra of D1 was attributed to the right hand side of the zero energy noise peak tail not being entirely eliminated by the low energy threshold (2 keV). At energies ≥ 11 keV the predicted to be detected spectra was in agreement with the experimentally detected ^{63}Ni β^- particle spectra of each pixel within the measured uncertainty, demonstrating uniformity in response across the two by two pixel array.

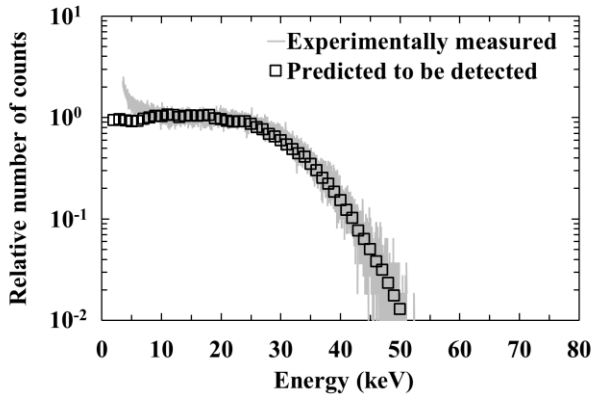

Fig. 5. Comparison between the experimentally measured ^{63}Ni β^- particle spectrum using pixel D1 (grey line) and that predicted from the simulations (squares). The experimentally measured spectrum was normalised to the mean number of counts detected per channel within the broadly flat 11 keV ≤ E ≤ 20 keV region of the experimentally measured spectrum. The predicted to be detected spectrum was normalised to the mean number of counts detected per channel within the broadly flat 1 keV ≤ E ≤ 20 keV region of the predicted to be detected spectrum. The associated uncertainties were smaller than the symbols.

5. A method to improve high energy response

Whilst the thickness of the detector's active region could be increased to improve the high energy response of the spectrometer, an alternative approach would be to use multiple thin detectors (e.g. as part of a pixel array) each of which has a different thickness of inactive absorber material in front of the pixel. This may be a useful approach in the case that thin commercial-off-the-shelf (COTS) detectors are being used by researchers who are unable to grow custom structures and procure suitable detectors with thick active layers from external suppliers. For example, in the instance of the presently reported four pixel array, one pixel may have no additional absorber, and the other three pixels may have progressively thicker aluminium layers (e.g. 20 µm, 100 µm, and 500 µm for D2, D3, and D4, respectively) deposited on top of them. A soft electron would be entirely attenuated by such Al layers, and would be thus prevented from reaching the pixel in question. However, for a high energy electron, the Al layer would only attenuate some of that electron's energy, with the remainder available to be absorbed in the pixel. Such Al layers could be tailored to be of appropriate thickness to reduce a portion of the incident spectrum's energy to that which is more readily detected by the thin detectors.

Monte Carlo simulations were conducted in order to identify the suitable Al layer thicknesses for example incident electron energies of 100 keV, 200 keV, and 500 keV. Al layers of varying thickness, directly atop the presently reported $Al_{0.2}Ga_{0.8}As$ detecting structure, were simulated at each electron energy of interest, using 4,000 electrons in each case. Two sets of simulations were conducted for each Al layer thickness in order to account for the areas covered and uncovered by the $Al_{0.2}Ga_{0.8}As$ p^+-i-n^+ mesa structure metal contact. They were combined in the appropriate proportions (see Section 3). Secondary electron generation was not included in the simulations. In the case of an incident electron energy of 100 keV, Al thicknesses of 5 µm, 10 µm, 20 µm, 30 µm, and 40 µm were simulated, see Fig. 6. The total number of detected counts from the resulting spectra, given 4,000 incident electrons, were then compared in order to establish the optimal Al thickness (greatest number of detected counts). Detected counts below an electron energy of 11 keV were not considered due to the mismatch between experimental and simulated results which was reported earlier (see Section 4.2).

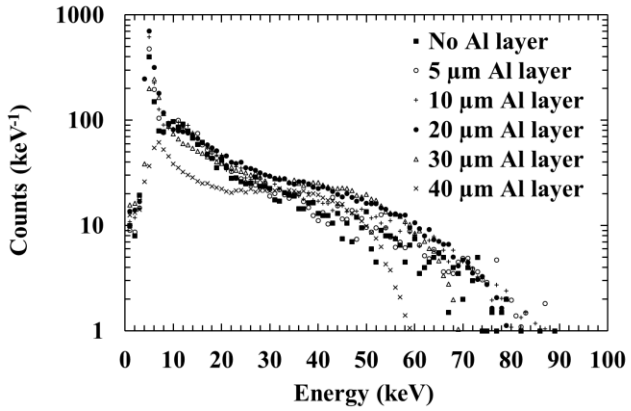

Fig. 6. Counts detected as a function of the deposited electron energy for a simulated $Al_{0.2}Ga_{0.8}As$ pixel with: no Al layer (filled squares); a 5 µm Al layer (empty circles); a 10 µm Al layer (plus signs); a 20 µm Al layer (filled circles); a 30 µm Al layer (empty triangles); a 40 µm Al layer (crosses). The associated uncertainties were omitted for clarity.

The resulting simulations showed that the number of counts detected from 4,000 incident 100 keV electrons was increased from 1291 ± 36 to 1664 ± 41 when a 20 µm Al layer is introduced. Similarly, the numbers of detected counts were increased from 397 ± 20 to 944 ± 31 given 4,000 incident 200 keV electrons, and from 101 ± 10 to 382 ± 20 given 4,000 incident 500 keV electrons, with the introduction of 100 µm and 500 µm Al layers, respectively. Fig. 7 shows how 20 µm, 100 µm, and 500 µm Al layers placed atop an $Al_{0.2}Ga_{0.8}As$ pixel improves the number detected counts for the spectrometer. The introduction of Al absorption layers atop the $Al_{0.2}Ga_{0.8}As$ structure was found to increase the E_{abs} of the spectrometer by 22 % (0.1238 ± 0.0020 to 0.1508 ± 0.0024) at 100 keV; 46 % (0.0296 ± 0.0005 to 0.0431 ± 0.0007) at 200 keV; and 20 % (0.0065 ± 0.0001 to 0.0078 ± 0.0001) at 500 keV, respectively.

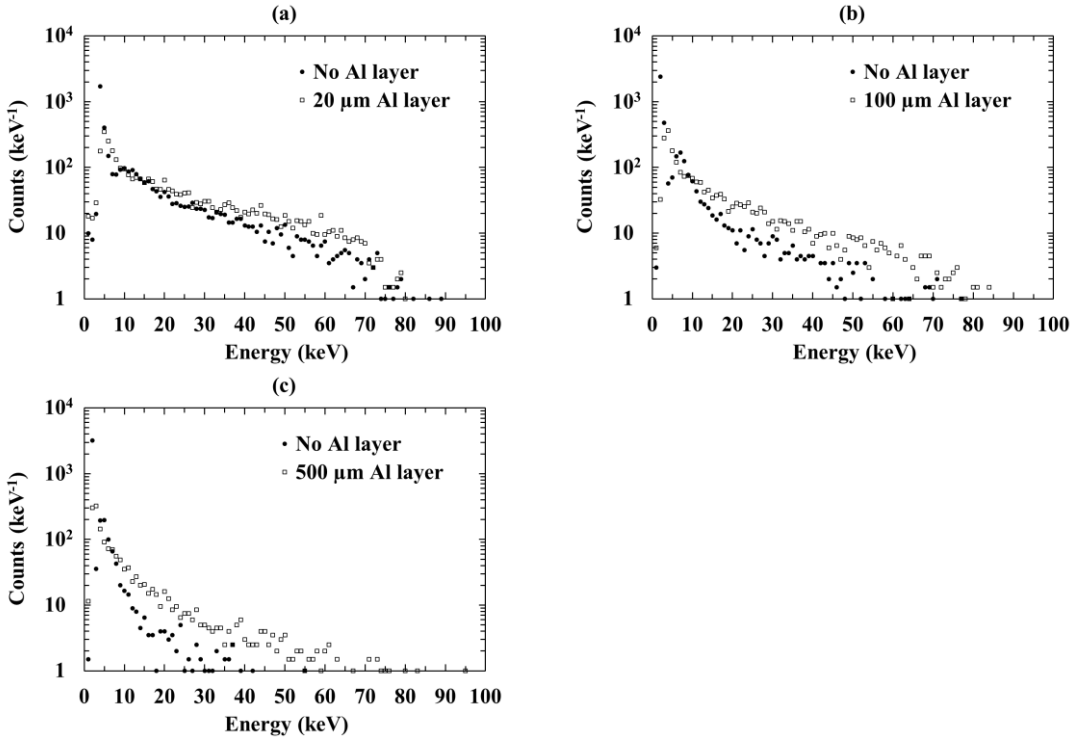

Fig. 7. Comparison of detected counts as a function of energy given 4,000 incident electrons of energy (a) 100 keV, (b) 200 keV, and (c) 500 keV, between an $Al_{0.2}Ga_{0.8}As$ pixel with the corresponding Al layer (empty squares), and without the Al layer (filled circles). The associated uncertainties were omitted for clarity.

6. Discussion of space science applications

The above results have demonstrated that this prototype $Al_{0.2}Ga_{0.8}As$ pixel array can be used for spectroscopic (FWHM at 5.9 keV = 0.76 keV ± 0.06 keV at 30 V applied to the detector, at 20 °C [27]) particle counting detection of electrons when coupled to suitable readout electronics. This is the first time $Al_{0.2}Ga_{0.8}As$ has been demonstrated for this application. Previous reports have shown $Al_xGa_{1-x}As$ to be potentially radiation hard [16][17][18]. Consequently, electron spectrometers with $Al_{0.2}Ga_{0.8}As$ detectors (either as single pixels or pixel arrays) may find use in future space missions to intense radiation environments. The benefits of inherently radiation-hard instrumentation may be demonstrated by considering the JEDI particle spectrometer on board the Juno spacecraft [3]. JEDI has an instrument mass of ≈ 1.4 kg plus ≈ 5 kg of radiation shielding [3]. If such an instrument was realisable using detectors and electronics of sufficient radiation tolerance that the shielding could be reduced in mass to the extent that the shielding only contributed 50% of the total instrument mass (i.e. an instrument mass of 1.4 kg plus 1.4 kg of shielding, for the JEDI example), two instruments could be flown within the same mass budget with 0.8 kg spare.

Indeed the development of radiation hard instrumentation, including electron spectrometers, for use in the Jovian system is a pressing matter. The magnetosphere of Jupiter is plasma-rich and of particular interest in contemporary space science. Jupiter's moon Io releases 1 Mg/s of O and S through volcanic eruptions [42]. Complex processes, involving magnetic field ruptures and plasma instabilities, accelerates this material, in addition to solar particles, to high energies, creating high energy ion and electron populations throughout Jupiter's magnetosphere. Measurements of these electrons and ions, including their associated energy, spatial, and angular distributions, can help studies of the nature and origin of the Jupiter's magnetic field, which is the largest and fastest rotating magnetic field in the Solar System after that of the Sun [42].

Whilst the detector array presented here is only a proof-of-concept prototype, it is informative to consider eventual use-cases for such instrumentation in order to direct future development. Since the predicted and measured ^{63}Ni β^- particle spectra were in agreement (see Section 4.2), a spectrum predicted to be detected within the near-Jupiter radiation environment was also considered. The omnidirectional electron flux (computed by ref. [43]) within the Jovian system, at a radial distance of 8.25 R_J (Jovian equatorial radius, R_J, = 71.4 Mm), was used to represent the soft electron (< 66 keV) radiation environment between the orbits of Io (5.90 R_J) and Europa (9.25 R_J), and is shown in Fig. 8. For clarity, and given the reported percentage of electron energy absorbed in the active region (i layer) of the pixel array (see Fig. 2), only electrons with energies in the range

1 keV – 66 keV were included in the prediction of the electron spectrometer's response in the Jovian environment. It should be noted that much higher electron energies (up to MeV energies) are also present within Jupiter's magnetosphere, albeit at reduced abundances.

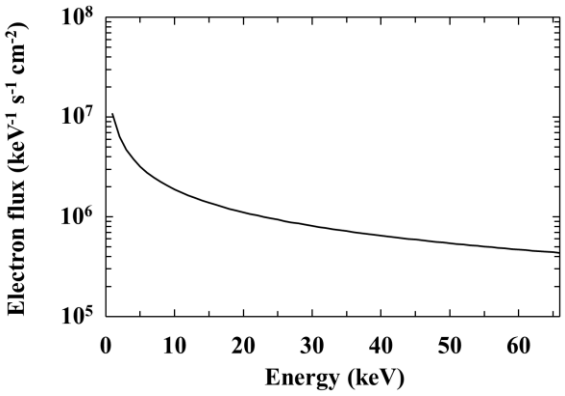

Fig. 8. Omnidirectional electron flux predicted at 8.25 R_J radial distance from Jupiter, as a function of energy, and calculated by ref. [43].

To convert the omnidirectional electron flux shown in Fig. 8 into the spectrum predicted to be incident on one $Al_{0.2}Ga_{0.8}As$ pixel of the type discussed above (excluding additional Al layers), the flux was halved (thus assuming that the detector is single sided) and multiplied by the area of one pixel (4×10^{-4} cm^2). The electron spectrum predicted to be usefully absorbed in the pixel's active region (assumed to be only the pixel's i layer) was then calculated by considering the weighted histogram of deposited electron energies as a function of incident electron energy, produced by the Monte Carlo simulations used to predict the percentage of electron energy absorbed in the active region of the detector (see Section 3), which accounted for energy losses within the dead layers of the pixel (the top Ohmic contact, the p^+ layer, the n^+ layer, and the substrate). Fig. 9 shows the spectrum predicted to be incident on the pixel and the spectrum predicted to be detected. The spectrometer's Fano noise, electronic noise, and any incomplete charge collection noise were excluded from the predictions, as were pixel edge effects. Electron energy losses within the top contact and p^+ layers explain the difference between the spectra in Fig. 9 at low energies, whereas the thinness of the active region explains the difference at high energies.

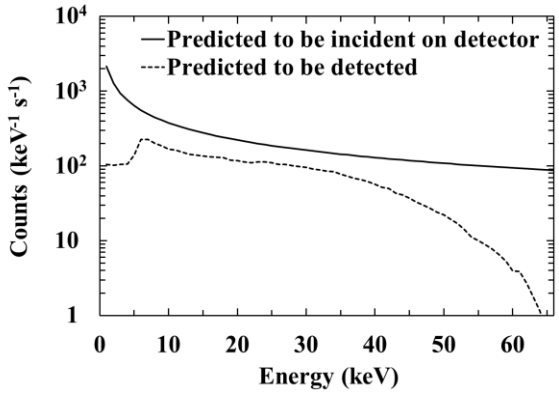

Fig. 9. Comparison between the electron spectrum (energy range, 1 keV to 66 keV) predicted to be incident on the detector (solid line) and spectrum expected to be detected (dashed line) at 8.25 R_J from Jupiter. The associated uncertainties were omitted for clarity.

It is also informative to consider the required spatial resolution for such a spectrometer. For a spectrometer moving on a spacecraft in orbit, the distance travelled in the time taken to collect an adequate (statistically significant) number of counts across the energy range of interest can be the limiting factor. Clearly, the percentage of electron energy absorbed in the i layer and area of the spectrometer's detector each play a part in this. The smallest auroral structures so far imaged at Jupiter are ≈ 80 km wide [44]. In addition, spacecraft orbiting Jupiter must travel at high speed due to Jupiter's large gravitational well (e.g. JUNO's orbital velocity ≈ 50 km s^{-1} [3]). Therefore, in order to spatially resolve similarly sized features at the spacecraft's orbit, the accumulation time of each spectra needs to be sufficiently short. In the case of JUNO, the electron spectrometer

was required to have an accumulation time of < 0.6 s [3]. Assuming a spacecraft speed of 50 km s^{-1}, this yields a spatial resolution of 30 km per spectrum. Given a single pixel of the 2 × 2 square pixel photodiode array reported here, and the expected omnidirectional electron flux at 8.25 R_J from Jupiter (8.41×10^7 keV^{-1} cm^{-2} s^{-1} within the energy range 1 keV to 66 keV), the total number of counts expected to be detected over an accumulation time of 0.6 s, would be 3.13×10^3 counts per pixel ± 43 counts per pixel.

Crudely speaking, given a source of constant excitation intensity, the detection of particles constitutes the counting of random events, and obeys the law of Poisson statistics. If the Omnidirectional electron flux predicted at 8.25 R_J radial distance from Jupiter is treated as such (an oversimplification, but useful for present purposes), then the relative statistical precision of the measurement can be approximated as $\approx 1/\sqrt{(I_m t)}$, where I_m is the counting rate and t is the real time of detection [45]. The total number of counts per pixel therefore has a relative statistical precision of ≈ 2 %. In order to identify and understand the incident electron flux from the detected spectrum, the statistical significance of accumulated counts across the investigated energy range needs to be high [46] and the electron environment must be modelled.

7. Conclusion

A prototype monolithic 2 × 2 square pixel $Al_{0.2}Ga_{0.8}As$ p^+-i-n^+ mesa photodiode array (each photodiode of area 200 µm by 200 µm, with a 3 µm i layer) was investigated for its utility as a direct detection electron detector operating uncooled at 20 °C. Each of the four $Al_{0.2}Ga_{0.8}As$ pixels were electrically characterised and their responses to illumination from a ^{63}Ni radioisotope β^- particle source were measured, with each pixel connected in turn to a custom-made low-noise charge-sensitive preamplifier and spectrometer readout chain. The results reported here are the first demonstration of $Al_{0.2}Ga_{0.8}As$ for direct detection electron spectroscopy.

The work was part of an ongoing programme to develop low-mass, low-volume, low-power, electron spectrometers, capable of operating within high temperature and intense radiation environments. The development of such instruments is motivated by anticipated future space science missions to extreme environments; such missions may include study of the plasma environments of the Jovian and Saturnian magnetospheres.

The percentage of electron energy absorbed in the active region (i layer) of the pixels of the array, and the ^{63}Ni β^- particle spectrum expected to be detected by each pixel of the array, were calculated using Monte Carlo simulations. The simulated spectra (i.e. those expected to be detected) were found to be in good agreement with those obtained experimentally. Thus, it was shown that the incident electron population from the ^{63}Ni β^- particle source at room temperature (20 °C) could be identified without any need for cooling.

As a possible option to improve the high energy response of the reported electron spectrometer, which was relatively thin, inactive Al absorber layers to be placed atop the detecting structure were investigated using Monte Carlo simulations. These simulations showed that the number of counts detected from 4,000 incident 100 keV electrons could be increased from 1291 ± 36 to 1664 ± 41 if a 20 µm Al layer was introduced. Similarly, the numbers of counts could be increased from 397 ± 20 to 944 ± 31 given 4,000 incident 200 keV electrons, and 101 ± 10 to 382 ± 20 given 4,000 incident 500 keV electrons, with the introduction of 100 µm and 500 µm Al layers, respectively. Thus the simulated E_{abs} of the spectrometer was found to increase by 22 % (0.1238 ± 0.0020 to 0.1508 ± 0.0024) at 100 keV; 46 % (0.0296 ± 0.0005 to 0.0431 ± 0.0007) at 200 keV; and 20 % (0.0065 ± 0.0001 to 0.0078 ± 0.0001) at 500 keV, respectively, when these inactive Al absorption layers were employed.

To inform future development of $Al_{0.2}Ga_{0.8}As$ detectors for space science applications, the electron spectrum predicted to be detected by a spectrometer employing an $Al_{0.2}Ga_{0.8}As$ photodiode of the type described within the near-Jupiter radiation environment was considered. Given a single pixel of the 2 × 2 array reported here, and the expected omnidirectional electron flux at 8.25 R_J from Jupiter (8.41×10^7 keV^{-1} cm^{-2} s^{-1} within the energy range 1 keV to 66 keV), the total number of counts expected to be detected over an accumulation time of 0.6 s would be 3.13×10^3 counts per pixel ± 43 counts per pixel. Assuming a spacecraft speed of 50 km s^{-1}, this accumulation time yields a spatial resolution of 30 km per spectrum, sufficient to investigate the electron environment features of the same size as the smallest auroral structures so far imaged at Jupiter (≈ 80 km wide [44]).

In future work, characterisation of thicker i layer $Al_{0.2}Ga_{0.8}As$ devices will be reported such that the percentage of electron energy absorbed in the active region (i layer) of the detector, and detected electron energy range, can be improved in order to satisfy the scientific objectives of future space science missions, potentially replacing current generation Si solid state detectors as the detector of choice for space based electron spectrometers.

Detectors of larger active area will also be investigated. In addition, the characterisation of $Al_xGa_{1-x}As$ of varying Al concentration will also be reported in order to investigate the relationship between Al concentration and response to illumination with β^- particles.

Acknowledgements

This work was supported in part by Science and Technology Facilities Council, UK, Grants ST/M004635/1, ST/R001804/1, and ST/P001815/1. M.D.C.W. acknowledges funding received in the form of a PhD scholarship from University of Sussex, UK. A.M.B. acknowledges funding from the Leverhulme Trust, UK, in the form of a 2016 Philip Leverhulme Prize. The authors are grateful to B. Harrison, R. J. Airey, and S. Kumar at the EPSRC National Centre for III-V Technologies for material growth and fabrication.

References

[1] Livi, S.A., McNutt, R., Andrews, G.B., Keath, E., Mitchell, D., and Ho, G., 2003, *The Energetic Particles Spectrometers (EPS) on MESSENGER and New Horizons*, Proceedings of the Tenth International Solar Wind Conference, American Institute of Physics, Vol. 679, pp. 838.

[2] Andrews, G.B., Zurbuchen, T.H., Mauk, B.H., Malcom, H., Fisk, L.A., Gloeckler, G., Ho, G.C., Kelley, J.S., Koehn, P.L., Lefevere, T.W., Livi, S.S., Lundgren, R.A., and Raines, J.M., 2007, *The Energetic Particle and Plasma Spectrometer Instrument on the MESSENGER Spacecraft*, Space Science Reviews, Vol. 131, pp. 523-556.

[3] Mauk, B.H., Haggerty, D.K., Jaskulek, S.E., Schlemm, C.E., Brown, L.E., Cooper, S.A., Gurnee, R.S., Hammock, C.M., Hayes, J.R., Ho, G.C., Hutcheson, J.C., Jacques, A.D., Kerem, S., Kim, C.K., Mitchell, D.G., Nelson, K.S., Paranicas, C.P., Paschalidis, N., Rossano, E., and Stokes, M.R., 2017, *The Jupiter Energetic Particle Detector Instrument (JEDI) Investigation for the Juno Mission*, Space Science Reviews, Vol. 213, pp. 289-346.

[4] Mcnutt, R.L., Livi, S.A., Gurnee, R.S., Hill, M.E., Cooper, K.A., Andrews, G.B., Keath, E.P., Krimigis, S.M., Mitchell, D.G., Tossman, B., Bagenal, F., Boldt, J.D., Bradley, W., Devereux, W.S., Ho, G.C., Jaskulek, S.E., Lefevere, T.W., Malcom, H., Marcus, G.A., Hayes, J.R., Moore, G.T., Perry, M.E., Williams, B.D., Wilson, P., Brown, L.E., Kusterer, M.B., and Vandegriff, J.D., 2008, *The Pluto Energetic Particle Spectrometer Science Investigation (PEPSSI) on the New Horizons Mission*, Space Science Reviews, Vol. 140, pp. 315-385.

[5] Schindler, K., 2007, *Physics of Space Plasma Activity*, Cambridge University Press, Cambridge, UK.

[6] Lauter, J., Protić, D., Förster, A., and Lüth, H., 1995, *AlGaAs/GaAs SAM-avalanche photodiode: An X-ray detector for low energy photons*, Nuclear Instruments and Methods in Physics Research Section A, Vol. 356, pp. 324-329.

[7] Barnett, A.M., Lioliou, G., and Ng, J.S., 2015, *Characterization of room temperature AlGaAs soft X-ray mesa photodiodes*, Nuclear Instruments and Methods in Physics Research Section A, Vol. 774, pp. 29-33.

[8] Silenas, A., Pozela, J., Pozela, K., Dapkus, L., and Juciene, V., 2006, *High spatial resolution graded-gap $Al_xGa_{1-x}As$ X-ray detector*, Nuclear Instruments and Methods in Physics Research Section A, Vol. 563, pp. 21-23.

[9] Adachi, S., 1985, *GaAs, AlAs, and $Al_xGa_{1-x}As$: Material parameters for use in research and device applications*, Journal of Applied Physics, Vol. 58, pp. R1-R29.

[10] Bertuccio, G., and Casiraghi, R., 2003, *Study of silicon carbide for X-ray detection and spectroscopy*, IEEE Transactions on Nuclear Science, Vol. 50, pp. 175-185.

[11] Lioliou, G., and Barnett, A.M., 2015, *Electronic noise in charge sensitive preamplifiers for X-ray spectroscopy and the benefits of a SiC input JFET*, Nuclear Instruments and Methods in Physics Research Section A, Vol. 801, pp. 63-72.

[12] Benkhoff, J., Van Casteren, J., Hayakawa, H., Fujimoto, M., Laakso, H., Novara, M., Ferri, P., Middleton, H.R., and Ziethe, R., 2010, *BepiColombo—Comprehensive exploration of Mercury: Mission overview and science goals*, Planetary and Space Science, Vol. 58, pp. 2-20.

[13] Emerich, C., Lamarre, J.M., Moroz, V.I., Combes, M., Sanko, N.F., Nikolsky, Y.V., Rocard, F., Gispert, R., Coron, N., Bibring, J.P., Encrenaz, T., and Crovisier, J., 1987, *Temperature and Size of the Nucleus of Comet p/Halley Deduced from IKS Infrared VEGA-1 Measurements*, Astronomy and Astrophysics, Vol. 187, pp. 839-842.

[14] Fraser, G.W., Carpenter, J.D., Rothery, D.A., Pearson, J.F., Martindale, A., Huovelin, J., Treis, J., Anand, M., Anttila, M., Ashcroft, M., Benkoff, J., Bland, P., Bowyer, A., Bradley, A., Bridges, J., Brown, C., Bulloch, C., Bunce, E.J., Christensen, U., Evans, M., Fairbend, R., Feasey, M., Giannini, F., Hermann, S., Hesse, M., Hilchenbach, M., Jorden, T., Joy, K., Kaipiainen, M., Kitchingman, I., Lechner, P., Lutz, G., Malkki, A., Muinonen, K., Näränen, J., Portin, P., Prydderch, M., Juan, J.S., Sclater, E., Schyns, E., Stevenson, T.J., Strüder, L., Syrjasuo, M., Talboys, D., Thomas, P., Whitford, C., and Whitehead, S., 2010, *The mercury imaging X-ray spectrometer (MIXS) on bepicolombo*, Planetary and Space Science, Vol. 58, pp. 79-95.

[15] Abbey, A.F., Bennie, P.J., Turner, M.J.L., Altieri, B., and Rives, S., 2003, *Cooling out the radiation damage on the XMM-Newton EPIC MOS CCDs*, Nuclear Instruments and Methods in Physics Research Section A, Vol. 513, pp. 136-142.

[16] Walker, A.W., Heckelmann, S., Tibbits, T., Lackner, D., Bett, A.W., and Dimroth, F., 2017, *Radiation hardness of AlGaAs n-i-p solar cells with higher bandgap intrinsic region*, Solar Energy Materials and Solar Cells, Vol. 168, pp. 234-240.

[17] Yoshida, S., Mitsui, K., Oda, T., and Yukimoto, Y., 1982, *Comparison of High Energy Proton Radiation Damages on AlGaAs/GaAs and Si Solar Cells*, Japanese Journal of Applied Physics, Vol. 21, pp. 27.

[18] Yamaguchi, M., 1995, *Radiation resistance of compound semiconductor solar cells*, Journal of Applied Physics, Vol. 78, pp. 1476-1480.

[19] Gladstone, G.R., Waite Jr, J.H., Grodent, D., Lewis, W.S., Crary, F.J., Elsner, R.F., Weisskopf, M.C., Majeed, T., Jahn, J.M., Bhardwaj, A., Clarke, J.T., Young, D.T., Dougherty, M.K., Espinosa, S.A., and Cravens, T.E., 2002, *A pulsating auroral X-ray hot spot on Jupiter*, Nature, Vol. 415, pp. 1000.

[20] Dunn, W.R., Branduardi-Raymont, G., Elsner, R.F., Vogt, M.F., Lamy, L., Ford, P.G., Coates, A.J., Gladstone, G.R., Jackman, C.M., Nichols, J.D., Rae, I.J., Varsani, A., Kimura, T., Hansen, K.C., and Jasinski, J.M., 2016, *The impact of an ICME on the Jovian X-ray aurora*, J Geophys Res Space Phys, Vol. 121, pp. 2274-2307.

[21] Branduardi-Raymont, G., Bhardwaj, A., Elsner, R.F., and Rodriguez, P., 2010, *X-rays from Saturn: a study with XMM-Newton and Chandra over the years 2002–05*, Astronomy and Astrophysics, Vol. 510, pp. A73.

[22] Atzei, A., Wielders, A., Stankov, A., and Falkner, P., 2007, *Overview of the ESA Jovian Technology Reference Studies*, ESA/ESTEC Technical Note, NL.

[23] Whitaker, M.D.C., Lioliou, G., Butera, S., and Barnett, A.M., 2016, *$Al_{0.2}Ga_{0.8}As$ X-ray photodiodes for X-ray spectroscopy*, Nuclear Instruments and Methods in Physics Research Section A, Vol. 840, pp. 168-173.

[24] Barnett, A.M., Bassford, D.J., Lees, J.E., Ng, J.S., Tan, C.H., and David, J.P.R., 2010, *Temperature dependence of AlGaAs soft X-ray detectors*, Nuclear Instruments and Methods in Physics Research Section A, Vol. 621, pp. 453-455.

[25] Whitaker, M.D.C., Butera, S., Lioliou, G., and Barnett, A.M., 2017, *Temperature dependence of Al0.2Ga0.8As X-ray photodiodes for X-ray spectroscopy*, Journal of Applied Physics, Vol. 122, pp. 034501.

[26] Barnett, A.M., Lees, J.E., and Bassford, D.J., 2013, *First spectroscopic X-ray and beta results from a 400 μm diameter $Al_{0.8}Ga_{0.2}As$ photodiode*, Journal of Instrumentation, Vol. 8, pp. P10014-P10014.

[27] Whitaker, M.D.C., Lioliou, G., and Barnett, A.M., 2018, *$Al_{0.2}Ga_{0.8}As$ 2 × 2 square pixel X-ray photodiode array*, Nuclear Instruments and Methods in Physics Research Section A, Vol. 899, pp. 106-114.

[28] National Semiconductor Corporation, *Metal Can Packages (TO-3/5/8/18/39/46/52/72)*, 1999.

[29] Hovington, P., Drouin, D., and Gauvin, R., 1997, *CASINO: A new monte carlo code in C language for electron beam interaction —part I: Description of the program*, Scanning, Vol. 19, pp. 1-14.

[30] Drouin, D., Hovington, P., and Gauvin, R., 1997, *CASINO: A new monte carlo code in C language for electron beam interactions—part II: Tabulated values of the mott cross section*, Scanning, Vol. 19, pp. 20-28.

[31] Lide, D.R., 2005, *CRC Handbook of Chemistry and Physics*, 85th ed., CRC Press, Boca Raton, Florida, USA.

[32] Joy, D.C., and Luo, S., 1989, *An empirical stopping power relationship for low-energy electrons*, Scanning, Vol. 11, pp. 176-180.

[33] Press, W.H., Teukolsky, S.A., Vetterling, W.T., and Flannery, B.P., 1986, *Numerical Recipes*, Cambridge University Press, Cambridge, UK.

[34] Casnati, E., Tartari, A., and Baraldi, C., 1982, *An empirical approach to K-shell ionisation cross section by electrons*, Journal of Physics B: Atomic and Molecular Physics, Vol. 15, pp. 155-167.

[35] Lioliou, G., Butera, S., Zhao, S., Whitaker, M.D.C., and Barnett, A.M., 2018, *GaAs Spectrometer for Planetary Electron Spectroscopy*, Journal of Geophysical Research: Space Physics, Vol. 123, pp. 7568-7580.

[36] Zhao, S., Lioliou, G., Butera, S., Whitaker, M.D.C., and Barnett, A.M., 2018, *Electron Spectroscopy with a Commercial 4H SiC Photodiode*, Nuclear Instruments and Methods in Physics Research Section A: Accelerators, Spectrometers, Detectors and Associated Equipment, Vol. 910, pp. 35 40.

[37] Butera, S., Lioliou, G., Zhao, S., Whitaker, M.D.C., Krysa, A.B., and Barnett, A.M., 2019, *InGaP electron spectrometer for high temperature environments*, Scientific Reports, Vol. 9, Art. No. 11096.

[38] Younglove, B.A., and Olien, N.A., 1985, *Tables of Industrial Gas Container Contents and Density for Oxygen, Argon, Nitrogen, Helium, and Hydrogen*, National Institute of Standards and Technology, Gaithersbury, Maryland, USA.

[39] Liu, Y.-P., Tang, X.-B., Xu, Z.-H., Hong, L., Wang, H., Liu, M., and Chen, D., 2015, *Influences of planar source thickness on betavoltaics with different semiconductors*, Journal of Radioanalytical and Nuclear Chemistry, Vol. 304, pp. 517-525.

[40] Bertuccio, G., Rehak, P., and Xi, D., 1993, *A novel charge sensitive preamplifier without the feedback resistor*, Nuclear Instruments and Methods in Physics Research Section A, Vol. 326, pp. 71-76.

[41] Pfaff, R.F., Borovsky, J.E., and Young, D.T., 2013, *Measurement techniques in space plasmas: Particles*, American Geophysical Union, Washington, USA, pp. 339-355.

[42] Grasset, O., Dougherty, M.K., Coustenis, A., Bunce, E.J., Erd, C., Titov, D., Blanc, M., Coates, A., Drossart, P., Fletcher, L.N., Hussmann, H., Jaumann, R., Krupp, N., Lebreton, J.P., Prieto-Ballesteros, O., Tortora, P., Tosi, F., and Van Hoolst, T., 2013, *JUpiter ICy moons Explorer (JUICE): An ESA mission to orbit Ganymede and to characterise the Jupiter system*, Planetary and Space Science, Vol. 78, pp. 1-21.

[43] Mauk, B.H., and Fox, N.J., 2010, *Electron radiation belts of the solar system*, Journal of Geophysical Research: Space Physics, Vol. 115.

[44] Ingersoll, A.P., Vasavada, A.R., Little, B., Anger, C.D., Bolton, S.J., Alexander, C., Klaasen, K.P., and Tobiska, W.K., 1998, *Imaging Jupiter's Aurora at Visible Wavelengths*, Icarus, Vol. 135, pp. 251-264.

[45] Jenkins, R., Gould, R.W., and Gedcke, D., 1995, *Quantitative X-ray Spectrometry*, 2nd ed., Marcel Dekker, New York, USA.

[46] Pfaff, R.F., Borovsky, J.E., and Young, D.T., 2013, *Measurement Techniques in Space Plasmas: Fields*, American Geophysical Union, Vol. 103, pp. 1-355.

Figure 1

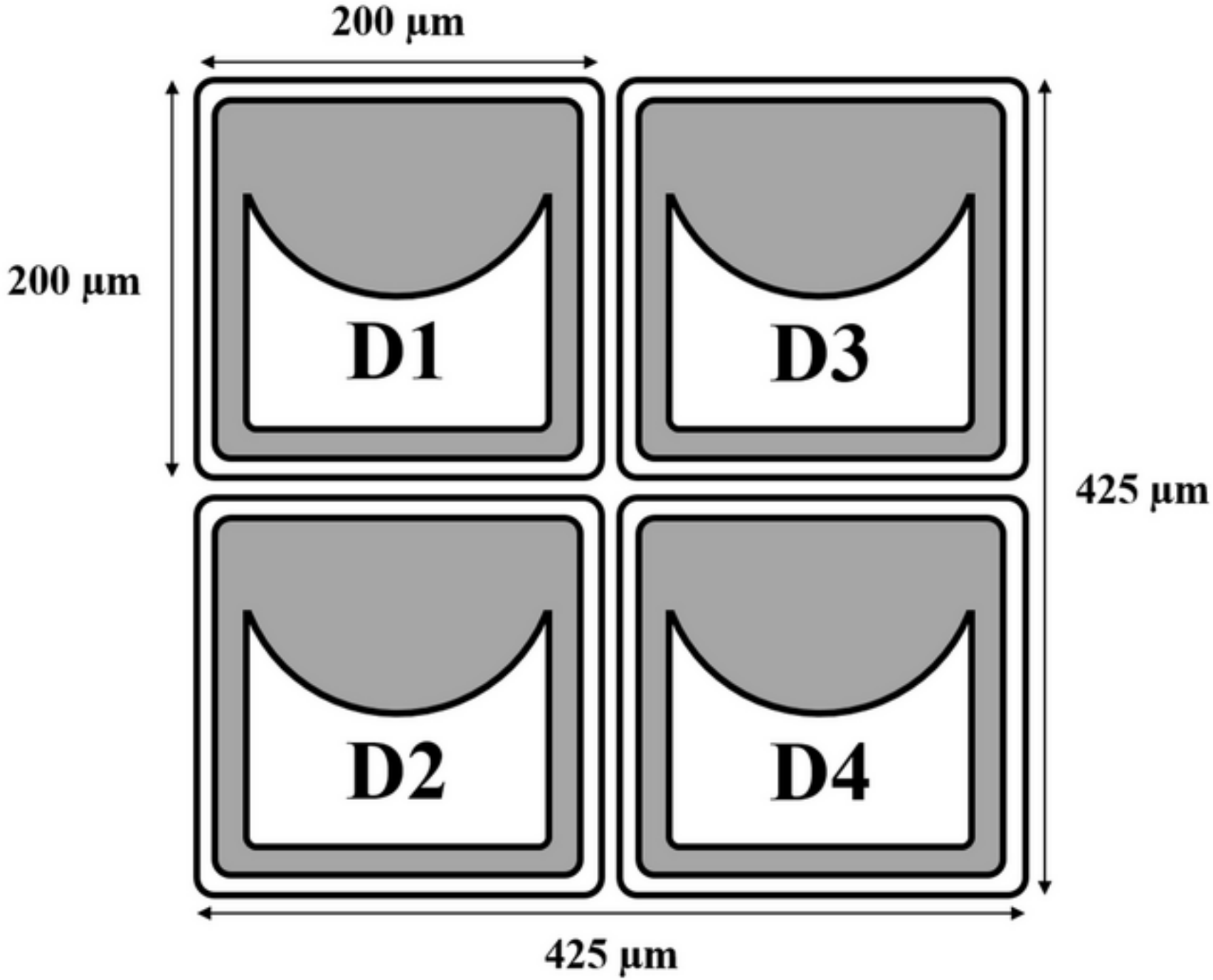

Figure 2a

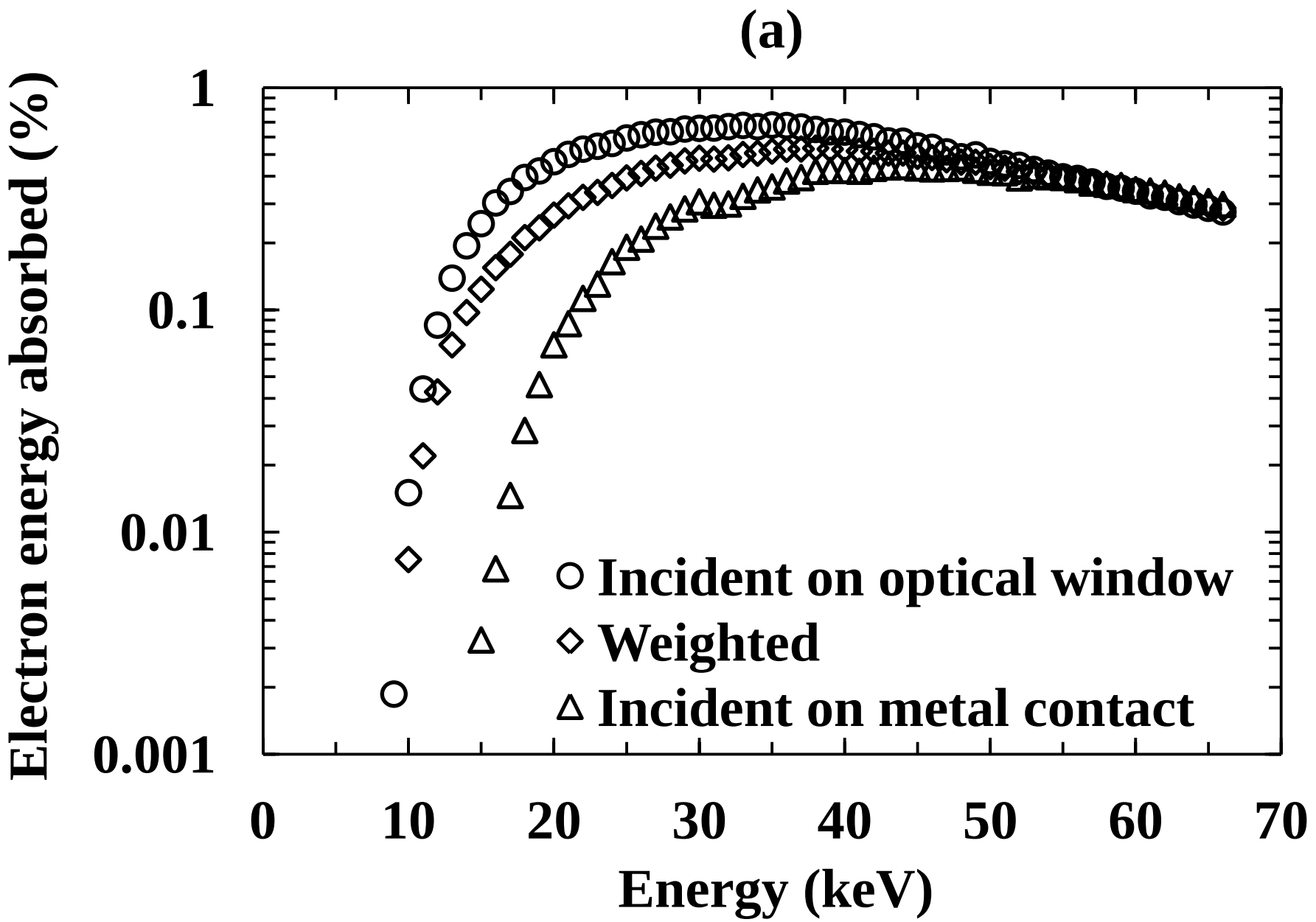
(a)
Electron energy absorbed (%)
1
0.1
0.01
0.001
0
10
20
30
40
50
60
70
Energy (keV)
Incident on optical window
Weighted
Incident on metal contact

Figure 2b

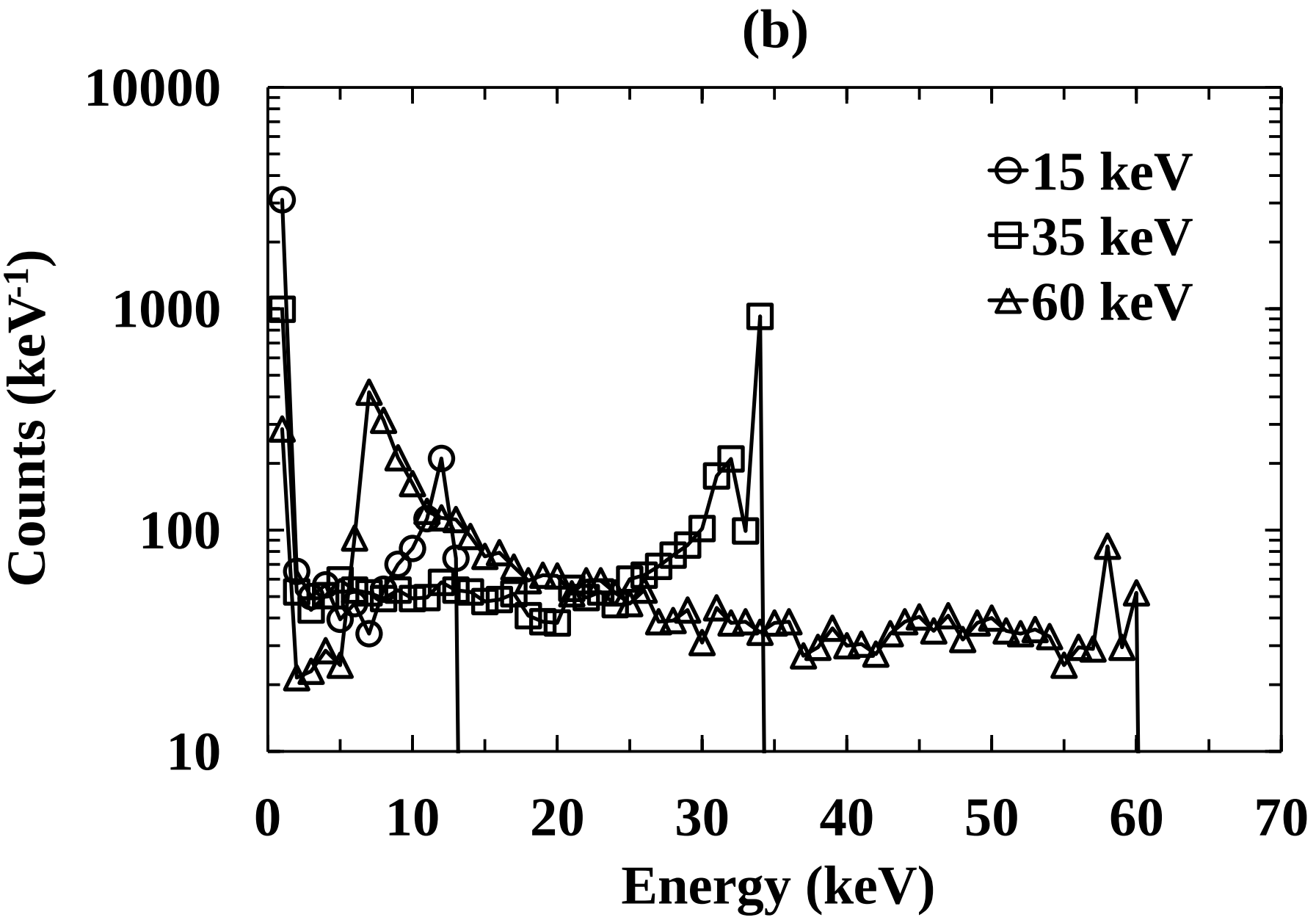
(b)
10000
1000
100
10
Counts (keV-1)
0
10
20
30
40
50
60
70
Energy (keV)
15 keV
35 keV
60 keV

Figure 3

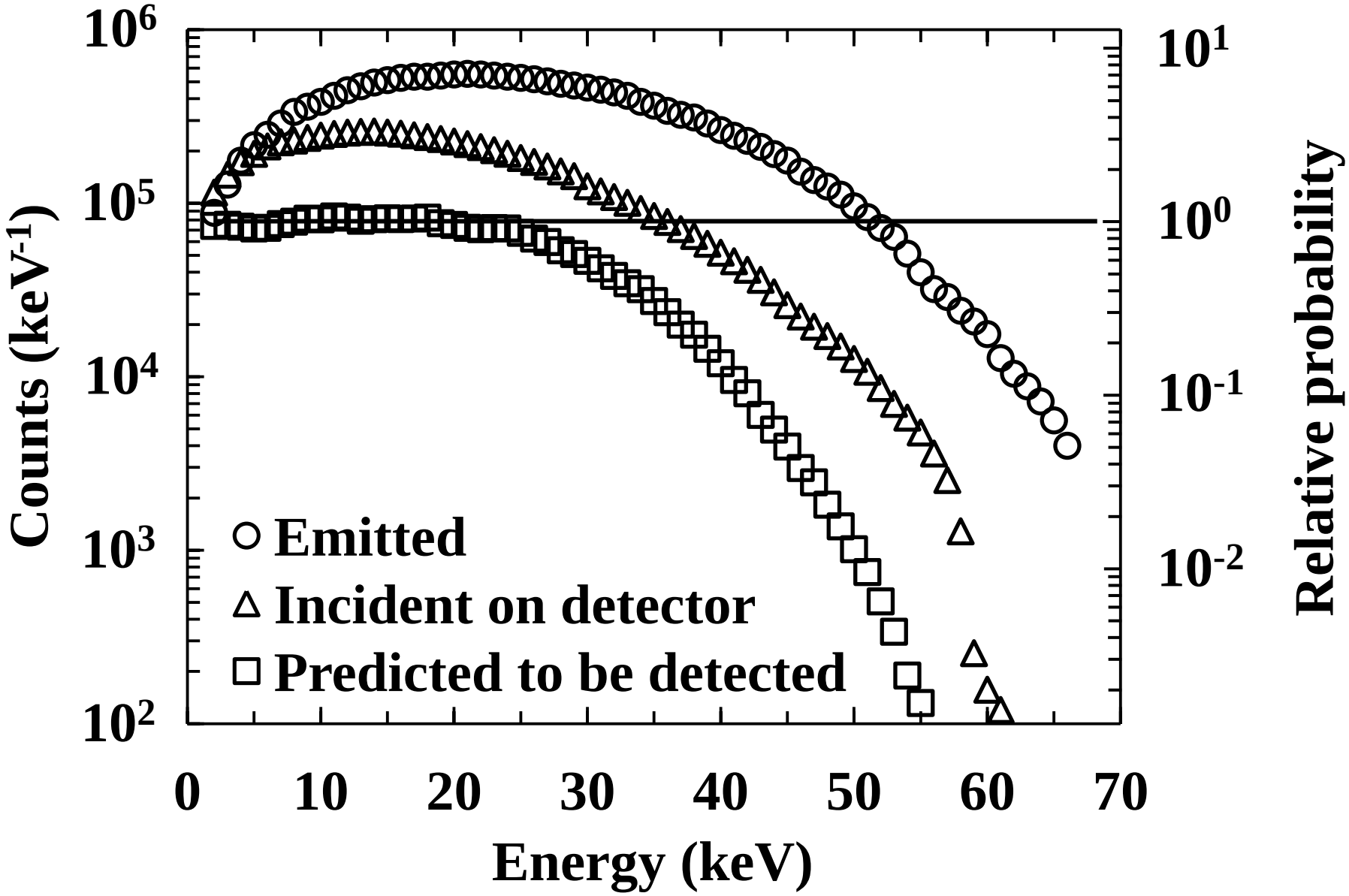
Counts (keV-1)
Relative probability
Energy (keV)
Emitted
Incident on detector
Predicted to be detected
10^6
10^5
10^4
10^3
10^2
10^1
10^0
10^-1
10^-2
0
10
20
30
40
50
60
70

Figure 4a

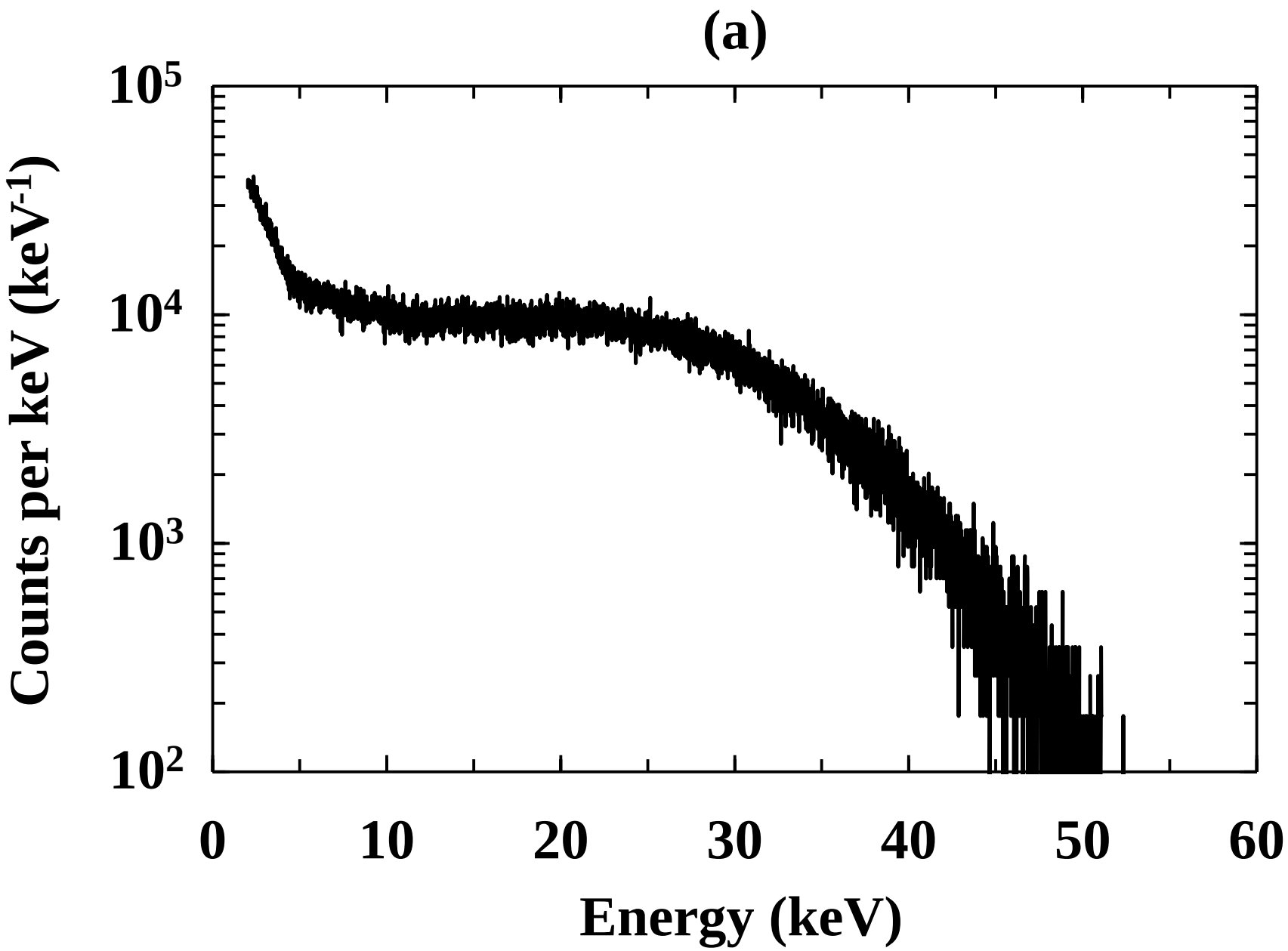
(a)
10^5
10^4
10^3
10^2
Counts per keV (keV^{-1})
0
10
20
30
40
50
60
Energy (keV)

Figure 4b

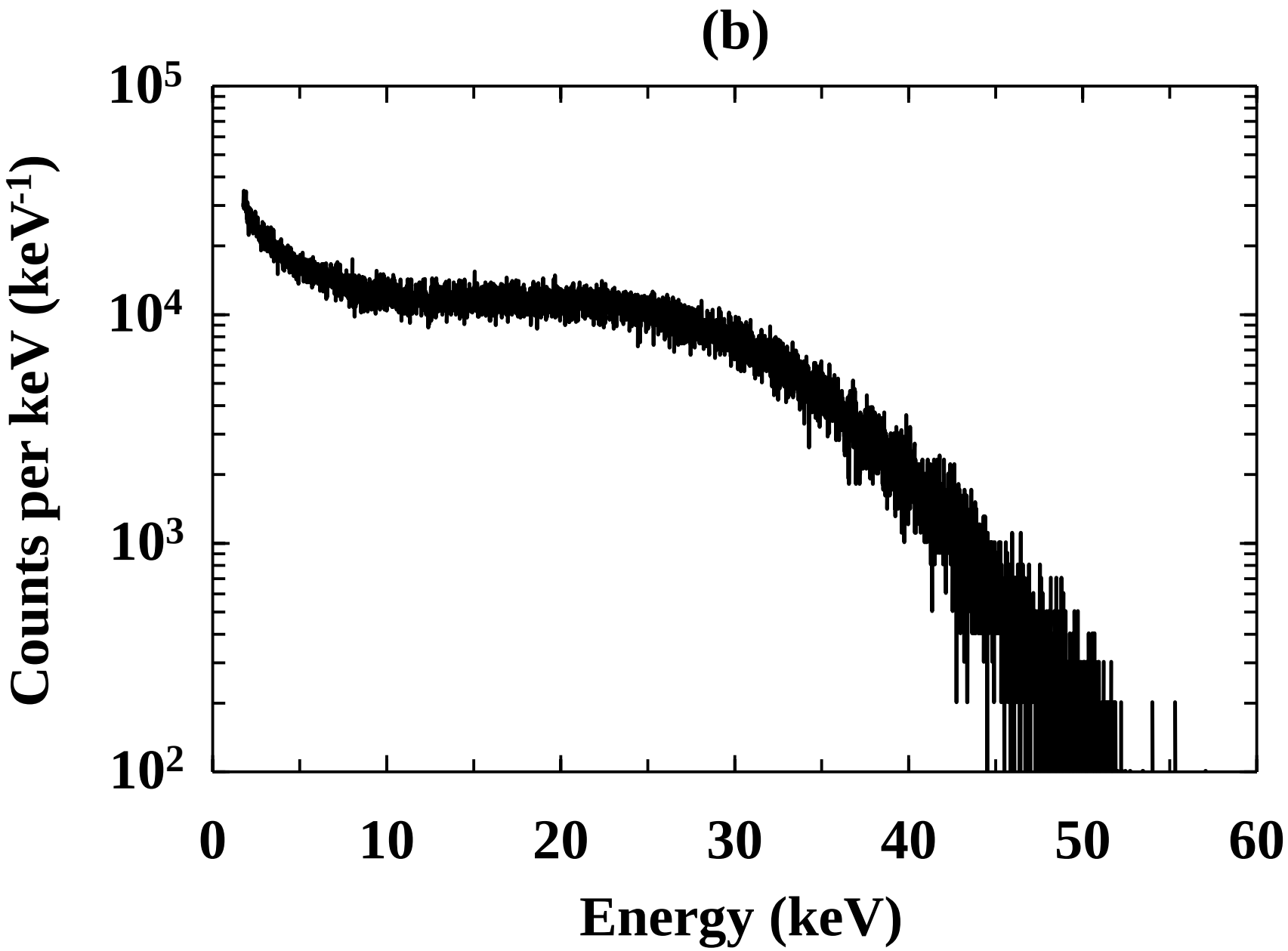
(b)
10^5
10^4
10^3
10^2
Counts per keV (keV^{-1})
0
10
20
30
40
50
60
Energy (keV)

Figure 4c

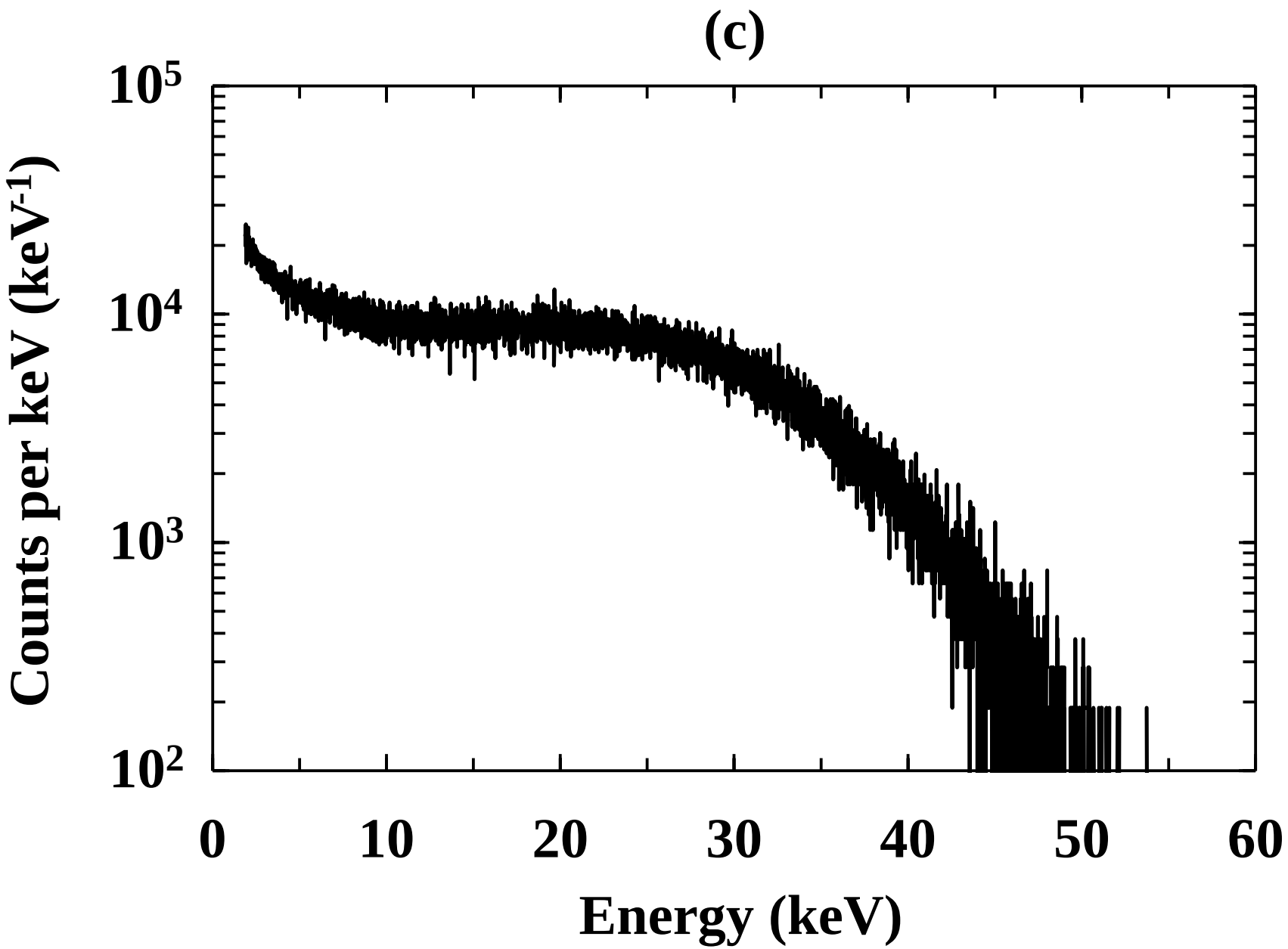
(c)
10^5
10^4
10^3
10^2
Counts per keV (keV^{-1})
0
10
20
30
40
50
60
Energy (keV)

Figure 4d

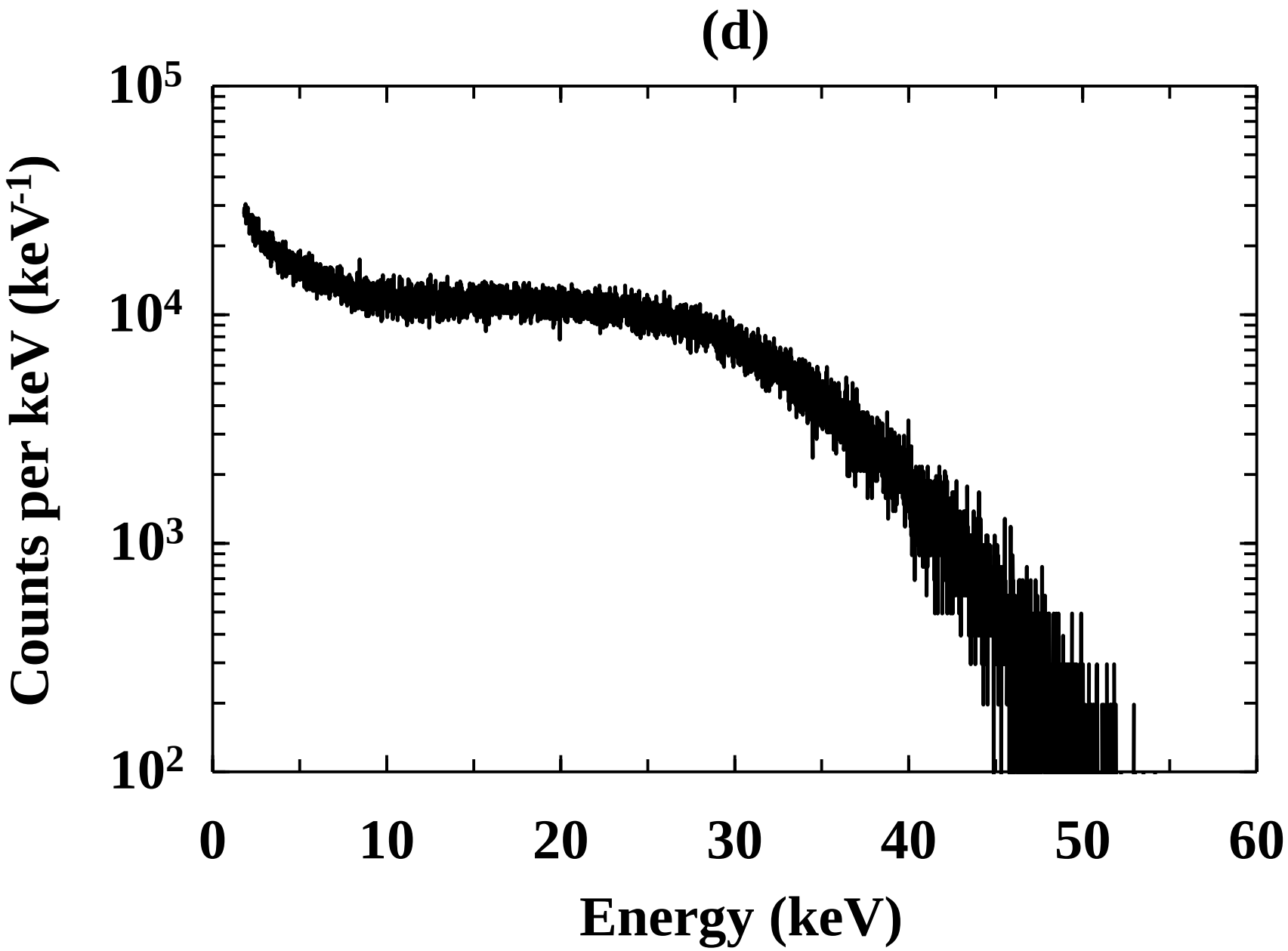
(d)
10^5
10^4
10^3
10^2
Counts per keV (keV^{-1})
0
10
20
30
40
50
60
Energy (keV)

Figure 5

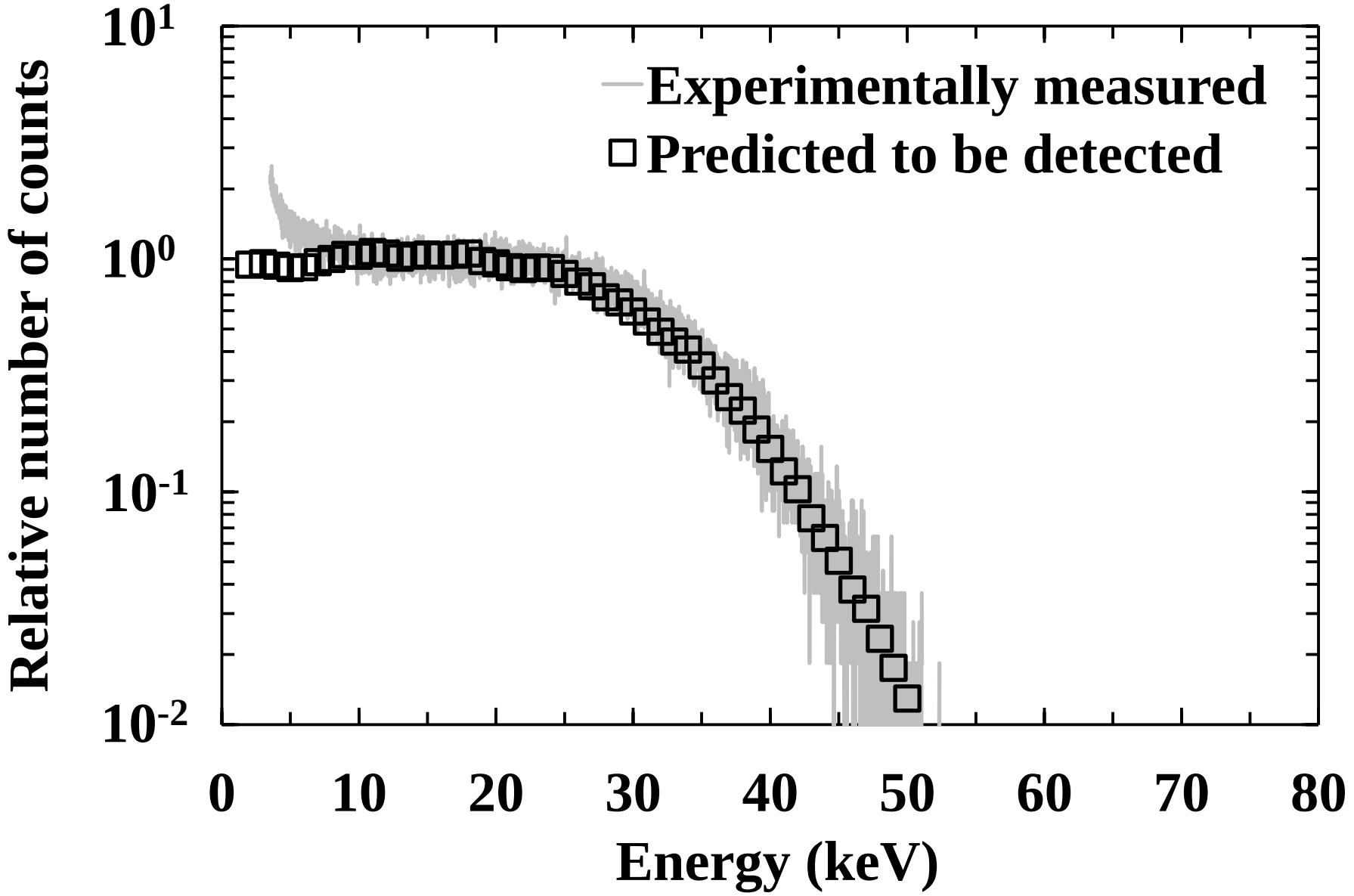
Relative number of counts
10^{1}
10^{0}
10^{-1}
10^{-2}
Experimentally measured
Predicted to be detected
0
10
20
30
40
50
60
70
80
Energy (keV)

Figure 6

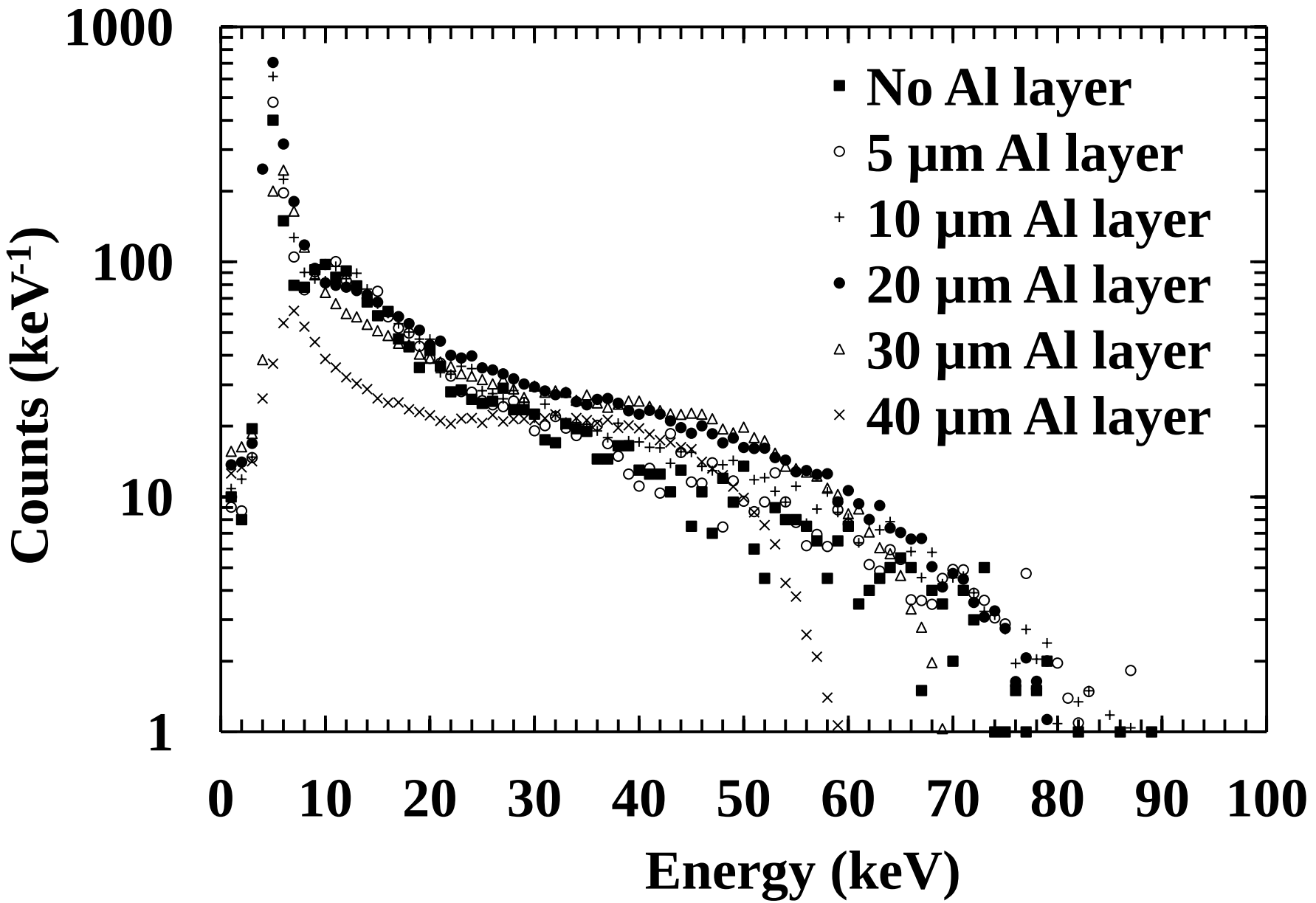
1000
100
10
1
Counts (keV-1)
0
10
20
30
40
50
60
70
80
90
100
Energy (keV)
No Al layer
5 µm Al layer
10 µm Al layer
20 µm Al layer
30 µm Al layer
40 µm Al layer

Figure 7a

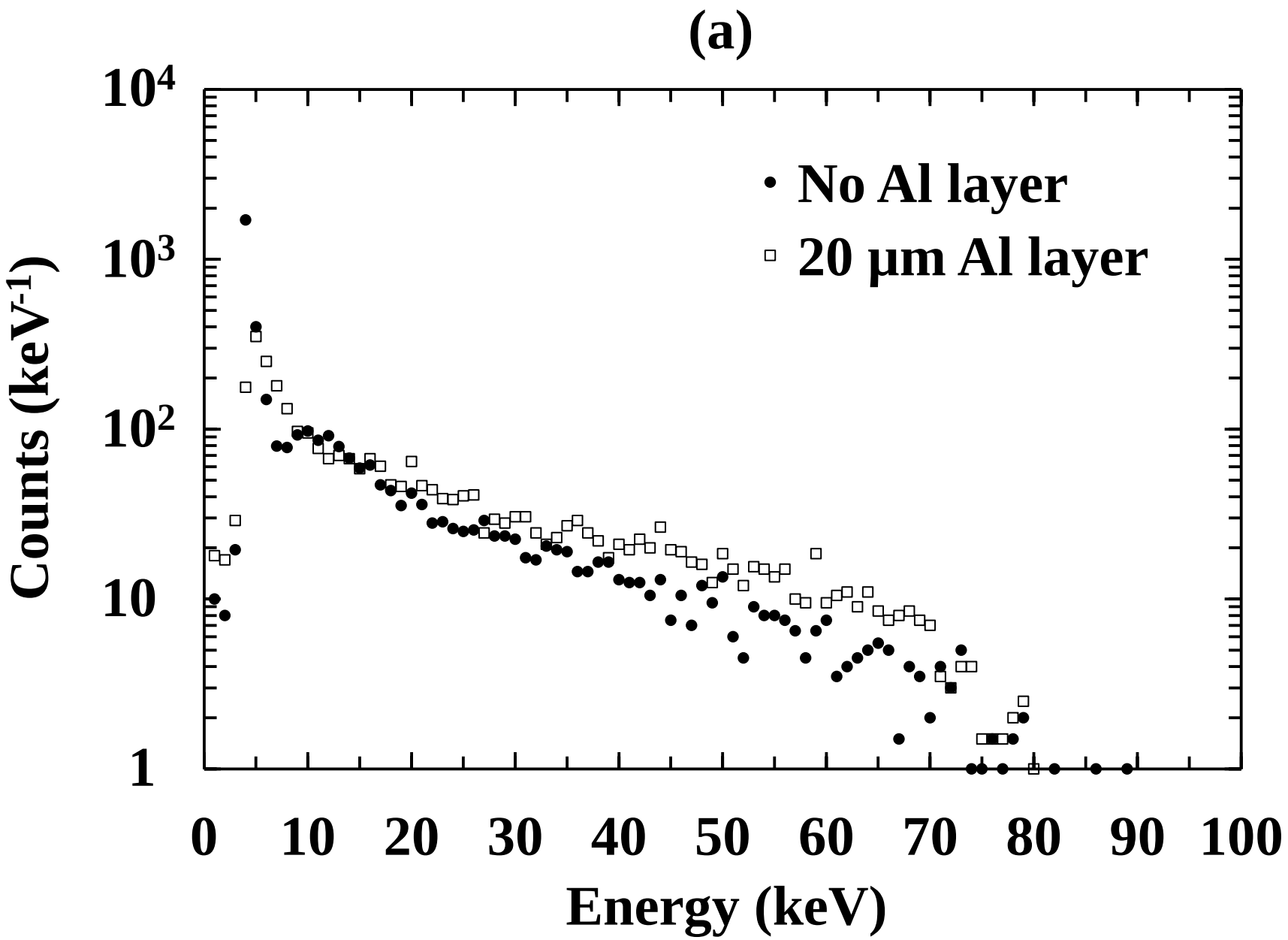
(a)
No Al layer
20 μm Al layer
Counts (keV-1)
Energy (keV)
10^4
10^3
10^2
10
1
0
10
20
30
40
50
60
70
80
90
100

Figure 7b

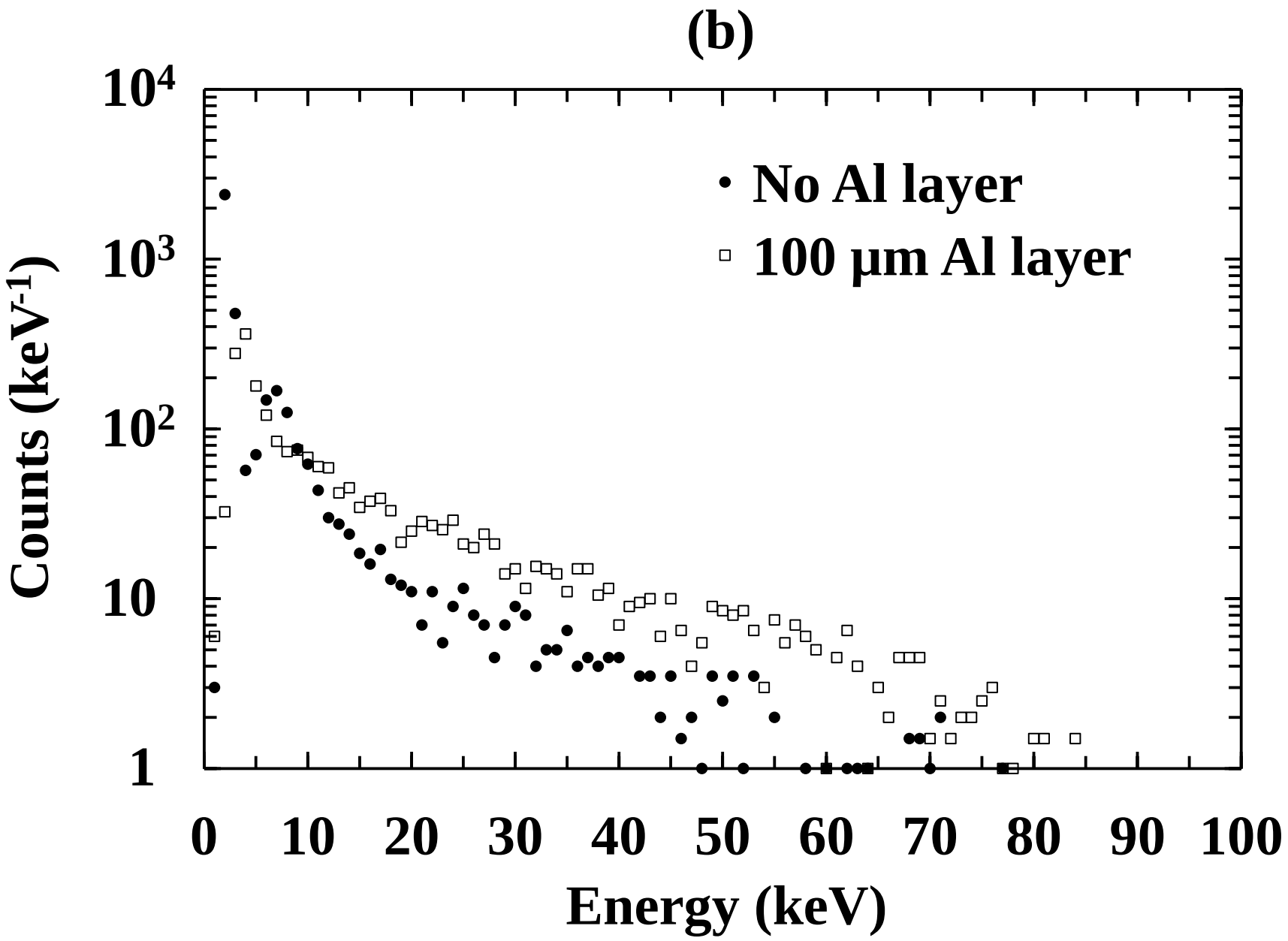
(b)
No Al layer
100 μm Al layer
Counts (keV-1)
Energy (keV)
10^4
10^3
10^2
10
1
0
10
20
30
40
50
60
70
80
90
100

Figure 7c

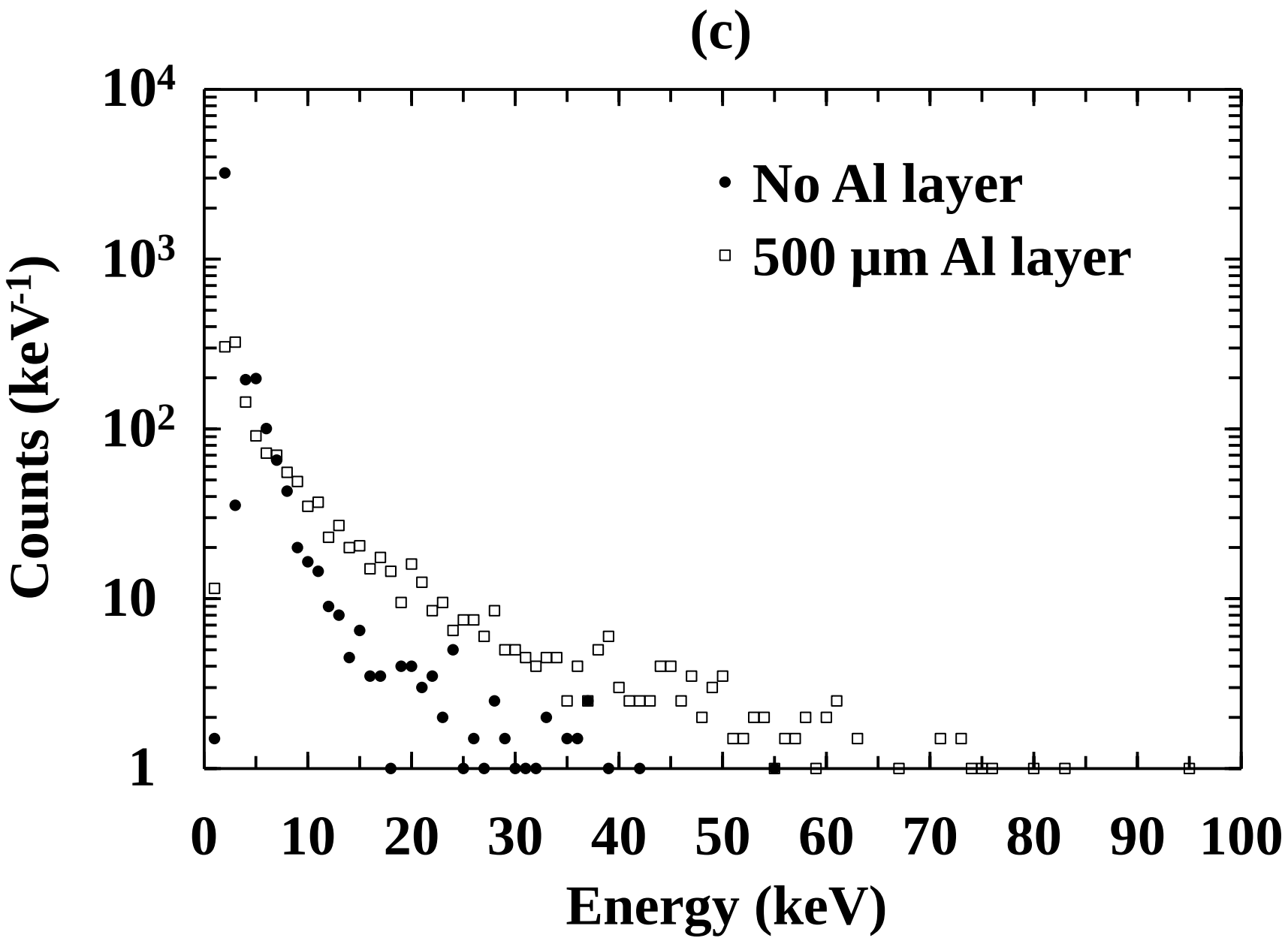
(c)
No Al layer
500 µm Al layer
Counts (keV-1)
Energy (keV)
10^4
10^3
10^2
10
1
0
10
20
30
40
50
60
70
80
90
100

Figure 8

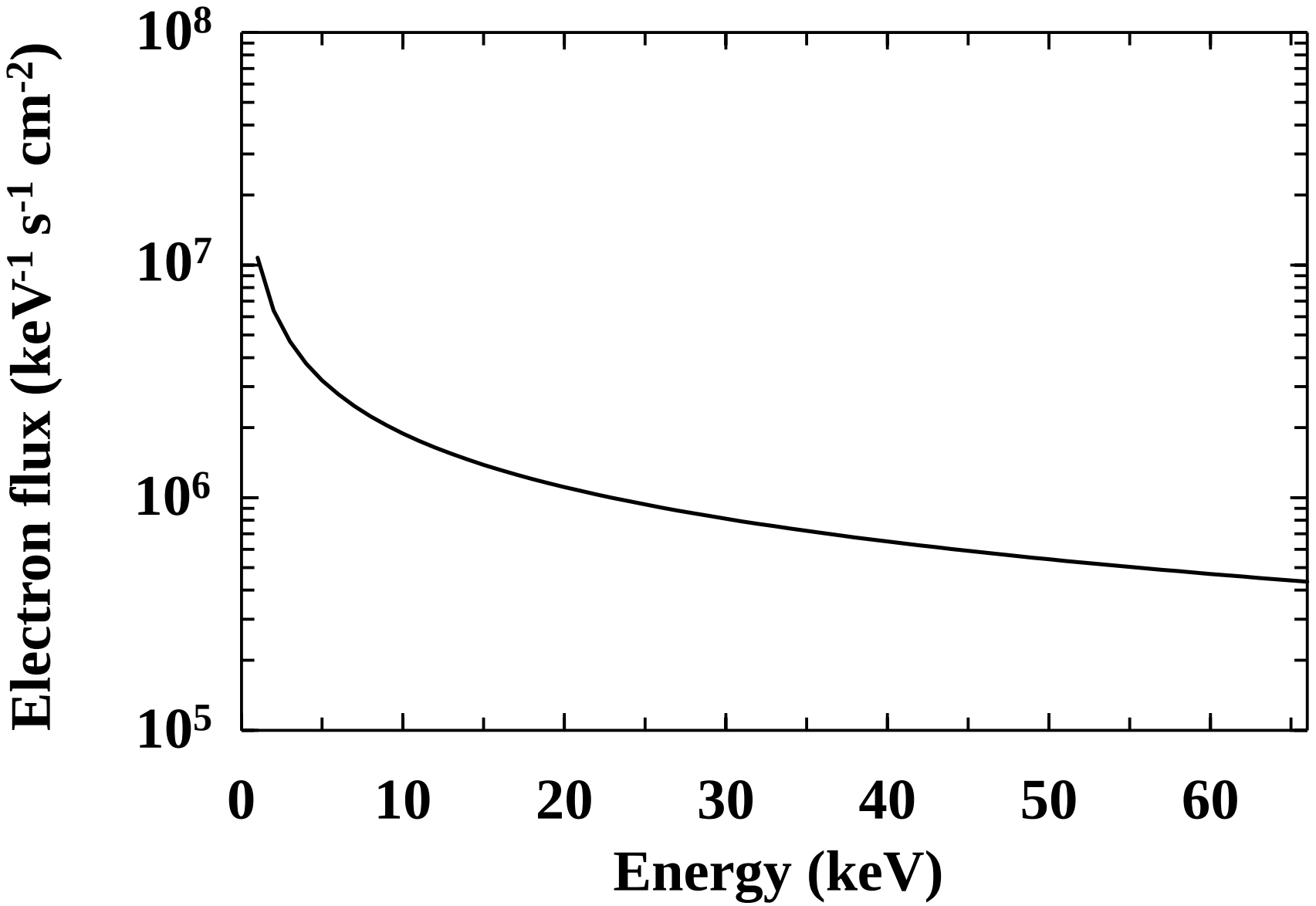
Electron flux (keV-1 s-1 cm-2)
10^8
10^7
10^6
10^5
0
10
20
30
40
50
60
Energy (keV)

Figure 9

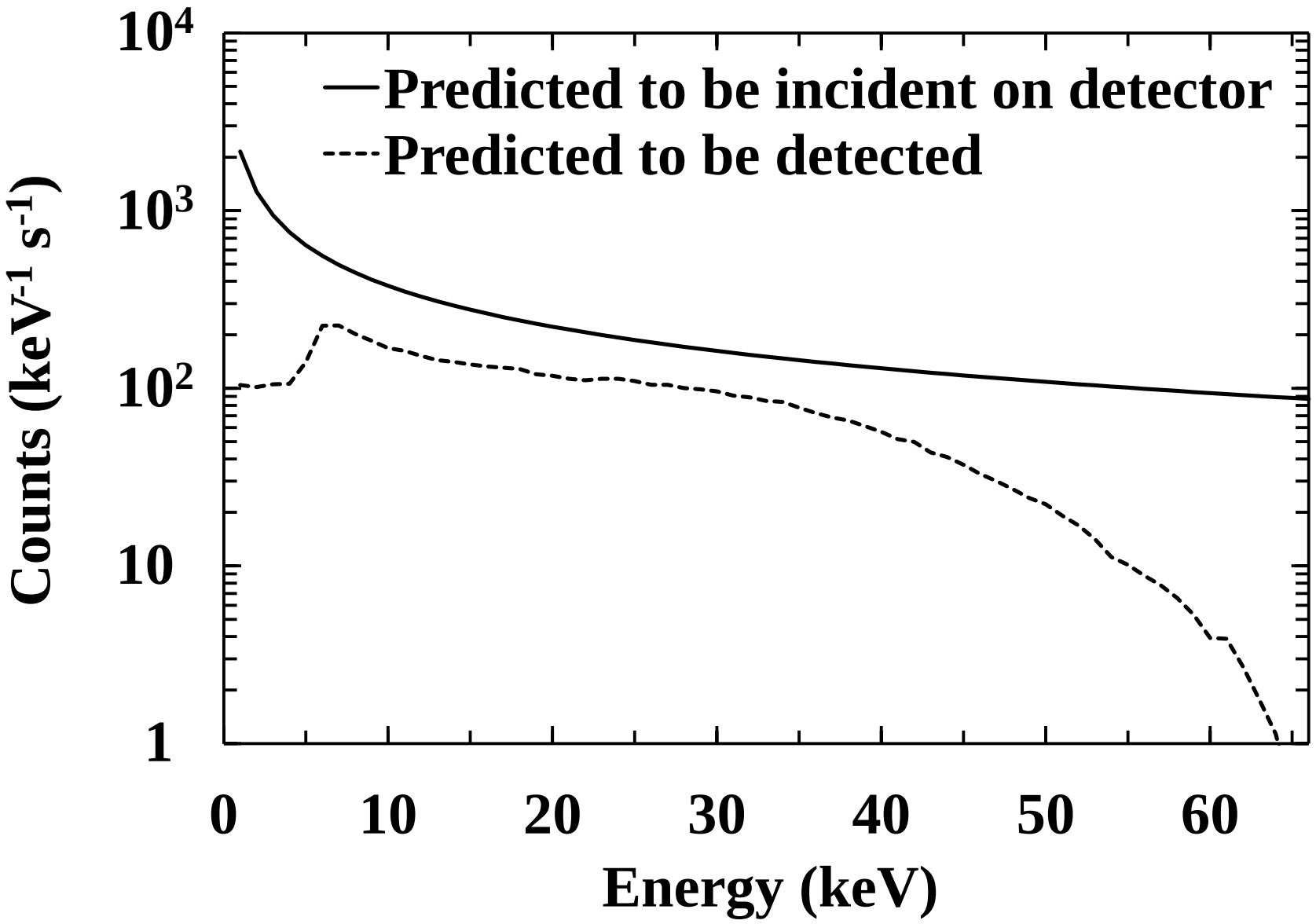
Predicted to be incident on detector
Predicted to be detected
Counts (keV-1 s-1)
10^4
10^3
10^2
10
1
0
10
20
30
40
50
60
Energy (keV)

Table 1

Material	Dopant	Dopant type	Thickness (μm)	Doping density (cm^{-3})
GaAs	Be	p	0.01	1×10^{19}
$Al_{0.2}Ga_{0.8}As$	Be	p	0.5	2×10^{18}
$Al_{0.2}Ga_{0.8}As$			3	Undoped
$Al_{0.2}Ga_{0.8}As$	Si	n	1	2×10^{18}
GaAs n^+ substrate				